ADVANCED MATERIALS
www.advmat.de

Nature-Inspired Liquid Crystal Polymer Actuators: From Alignment Regulation to Nano-composition

*Xiaoyu Zhang, Ziyue Yang, and Yanlei Yu**

Liquid crystal polymers (LCPs) that possess crosslinked networks and ordered alignment of mesogens are renowned for their large and reversible anisotropic deformation in response to external stimuli, which holds great potential in the burgeoning field of nature-inspired actuators and robots. Continuous efforts have been made in revealing the interplay between materials chemistry, processing, and alignment of LCPs, to broaden the actuation modes and enhance the actuation performance toward practical utilization. In this review, the advances in nature-inspired LCP actuators is focused with special attentions devoted in their mesogen alignment and the macroscopic geometry. Since the mesogen alignment is vital for the attainable actuation modes, the methods for alignment regulating are detailly combed, including surface-enforced alignment, field-assisted alignment, mechanical alignment, rheological alignment, and self-assembly. Subsequently, the composition of nanomaterials is futher surveyed in LCP actuators with a focus on enhancing the actuation performance. Finally, perspectives on the current challenges and potential development trends are discussed, which may shed light on future investigations.

1. Introduction

Biological muscles have evolved to operate complex actuations in dynamic environments, which are challenging but still appealing to replicate in synthetic systems. The artificial muscle made of intelligent shape-changing polymer is a burgeoning area of research, in particular, for the application in nature-inspired actuators and robotics.[1–3] Beyond the compliance and adaptivity to surroundings, the intelligent shape-changing polymers also undergo a predetermined geometric change for actuation upon external stimuli, thus intrinsically integrating perception and actuation. This life-like characteristic, along with the stride of structural and morphological biomimicry,[4–8] bring artificial actuators closer to living organisms.

As a competitive kind of stimuli-responsive polymers for artificial muscles, the crosslinked liquid crystal polymers (CLCPs) with ordered mesogen alignment attract wide research attention due to their sizable and reversible anisotropic deformation.[9,10] As early as 1969, the potentials of liquid crystal elastomers to perform expansile-contractile deformation as muscle fibers has been predicted by Pierre-Gilles de Gennes,[11] which sparked a wave of interests in exploiting CLCPs for actuators (**Figure 1**). Thereafter, continuous efforts were devoted to revealing the interplay between materials chemistry, processing, and alignment, while attempts were made to broaden the actuation modes and enhance the actuation performance accordingly.

A feature of CLCPs is quite conspicuous from the perspective of actuator applications, that is, the alignment-dependent deformation.[12–14] In the biological muscles, the spatial arrangement of muscle fibers has a decisive influence on the motions of muscles. Similarly, the ordered alignment is the prerequisite of the anisotropic deformation of CLCPs, and the alignment of mesogens plays a critical role on the attainable actuation modes. Therefore, how to effectively regulate the mesogen alignment as desired while construct bionic structures and morphologies, remains a common theme for nature-inspired LCP actuators. Up to date, a variety of alignment methods have been developed, including surface-enforced alignment, field-assisted alignment, rheological alignment, mechanical alignment, and self-assembly. Wherein, the surface-enforced and field-assisted aligning possess the merits to regulate the mesogen alignment with higher freedom and accuracy, while the others hold the precedence in facilitating actuators with more stereoscopic geometries. Since the LCP actuators featuring 2D thin films constituted the majority of studies in the past decades, the design of actuation modes mainly focused on improving the diversity and complexity of mesogen alignment for better mimicking their natural counterparts. In this case, the surface-enforced and field-assisted aligning were preferred because they allowed manifold mesogen alignments from monodomain to customized 3D patterns.

The turning point in the research of aligning methods is partly attributable to the commercialized production of polymerizable mesogenic monomers, the new materials chemistry on the basis of aza/thiol-Michael addition,[15,16] and the application of 3D printing to LCP actuators.[17–20] Benefiting from the simplification of both synthesis and processing, the threshold to

X. Zhang, Z. Yang, Y. Yu
College of Smart Materials and Future Energy
State Key Laboratory of Molecular Engineering of Polymers
Fudan University
2005 Songhu Road, Shanghai 200438, China
E-mail: ylyu@fudan.edu.cn

The ORCID identification number(s) for the author(s) of this article can be found under https://doi.org/10.1002/adma.202509892

DOI: 10.1002/adma.202509892

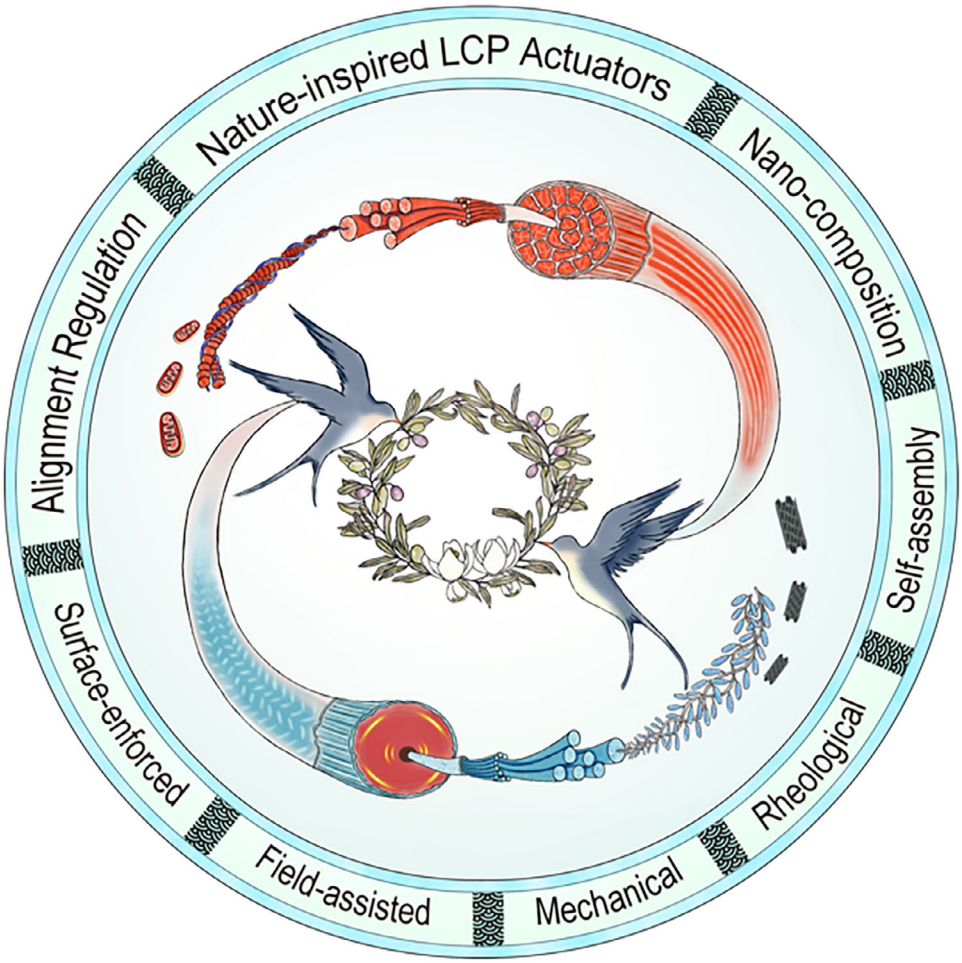

Figure 1. The concept illustration. A real swallow, powered by biological muscles, and an artificial swallow powered by liquid crystal polymer (LCP) actuators jointly hold in their beaks a budding olive wreath symbolizing wisdom, which represents that the development of nature-inspired LCP actuators appears as a bridge between artificial systems and the natural biological intelligence. Similar to the myofilaments that assemble into orderly arranged muscle fibers in biological muscles, the mesogens assemble into an ordered LC phase for artificial LCP muscles, with corresponding X-ray diffraction (XRD) pattern shown in the cross sections. Moreover, the mitochondria and carbon nanotubes (CNTs) serve as the typical representatives of inner energy conversion systems for biological muscles and LCP actuators, respectively.

utilize CLCPs for actuator applications dramatically decreases, thus drawing growing interest from researchers beyond LCP chemists. The interdisciplinary research on LCP actuators has boosted the predictable and designable actuations that broke traditional imagination, while its thriving development has also proposed higher requirement to the attainable complexity of macroscopic structures. Consequently, the rheological alignment, mechanical alignment, and self-assembly have gradually gained more widespread use, due to their superiority in geometry design. Currently, the rheological and mechanical alignment exhibit as the most popular methods, since they are compatible with CLCPs synthesized by commercial mesogenic monomers. As for the self-assembly, it offers huge freedom to the structure design of LCP actuators, and pioneer in the fabrication of actuators with microscale complicated 3D structures. Nevertheless, the high-threshold synthesis of the required materials results in remarkable obstacles to its promotion.

In addition to the arrangement of muscle fibers which provides the structural basis of motions, the power density also plays a non-negligible role in achieving various activities of biological muscle, since it directly impacts the maximum force output and contraction velocity. Similarly, the actual power density of CLCPs is another critical property for realizing targeted actuations apart from the mesogen alignment, especially for the motions that require a sharp increase of energy supply in a short time. The composition of biological muscles may give some inspirations on achieving desired power density, that is, they possess inner energy conversion systems, such as the mitochondria, for high-efficient energy supply. Given that, the nano-composition appears as an appealing approach for tuning the power density of LCP actuators, due to the excellent energy conversion efficiency of certain nanomaterials.[21,22] Generally, the incorporations of nanomaterials facilitate the synergistic optimization of power density and mechanical property, which contribute to the construction of robust LCP actuators with high actuation performance. By further combining with the design of macroscopic structure, the nanocomposites actuators have achieved a series of non-trivial actuation modes, such as jumping and high-power

oscillation. Since the nano-composition enables the CLCPs to accomplish actuations that are difficult for pure CLCPs in a convenient way, it is expected to gain more prevalent use in LCP actuators for extending their usage scenarios.

Here, we provide an overview of the development and the cutting edge of nature-inspired LCP actuators. The basic concepts of CLCPs and the mechanisms of their stimuli-responsive deformation are presented at the beginning. Afterward, we detail the alignment regulation coupled with the obtained actuators. Especially, how the mesogen alignment and the macroscopic geometry cooperatively contribute to the final nature-inspired actuations are highlighted throughout the text. Furthermore, the nano-composition used for enhancing the actuation performance of LCP actuators is outlined, along with the demonstration of intriguing motions that require high power density and mechanical robustness. Within this framework, we provide an outlook discussing current challenges and emerging research opportunities of LCP actuators.

2. Mechanism of Reversible Deformation of CLCPs

The initial CLCPs featured monodomain alignment and the geometry of 2D films, which generally exhibited simple contraction-expansion or bending-unbending deformation upon external stimuli. As early as 1991, Finkelmann et al. proposed a two-step crosslinking method to prepare aligned polysiloxane CLCPs.[23] The vinyl groups react two orders of magnitude faster than methacryloyl groups according to the kinetic studies, thus providing enough time interval between the two crosslinking reactions for mechanical alignment. The lightly-crosslinked solid mesogenic precursor was created by the first crosslinking, whose mesogens were uniformly aligned by mechanical stretching and fixed by the second crosslinking (**Figure 2a**).[24,25] This method allows convenient fabrication of uniaxially aligned CLCP fibers and films from the millimeter to centimeter scale.

When discussing the mechanism of mechanical alignment, a well-known feature of LCPs must be pointed out at first: the chain conformation spontaneously forms a polydomain structure at the liquid crystal phase, and demonstrates local anisotropy even without any alignment treatment. This phenomenon is attributed to the self-organization of mesogens, which directionally extend their attached polymer chains within a micron-sized domain (usually 1–2 µm).[26] The widely-studied nematic LCPs usually exhibit prolate local domains where the mesogens arrange along the polymer chains, while the smectic mesogenic polymers and several nematic side-chain end-on LCPs form oblate local domains with mesogens aligning vertical to the polymer chains (Figure 2b).[27–29] The microdomains in the initial polydomain LCPs align in disorder, therefore the mesogen alignment shows isotropy at macroscopic scale. When subjected to external force, the long axis of microdomains (the direction of polymer chains) align along the loading direction, thereby the mesogens are aligned as well. Generally, the alignment of LCPs featuring prolate domains is parallel to the loading direction, while the mesogens of LCPs with oblate domains align perpendicular to the loading direction. Specially, with considerable external force that exceeds a threshold stress, the microdomains alter from the initial oblate conformation to prolate due to the sliding between mesogens, thus leading to alignment along the loading direction.[27,30]

During the same period, Broer et al. reported a one-step crosslinking method to prepare aligned acrylate CLCPs.[31] The low-viscosity precursors containing mesogenic monomers and crosslinkers were introduced into the LC cell through capillary action, where the mesogens were aligned by surface anchoring and then fixed by chemical crosslinking (Figure 2c).[32] Generally, the LC cells consist of spacers and two glass substrates coated with alignment layers (Figure 2d), while the surface morphology and physicochemical properties of alignment layers determine the director orientation. Homogeneous director orientation (1D) is available via the anchoring effect of alignment layers with microgrooves, where the mesogens align along the direction of the microgrooves to minimize the surface energy.[33–35] Homeotropic director orientation (1D) is attainable with alignment layers featuring low polarity component, attributed to the strong repulsion between the mesogens and alignment layers.[36–38] The geometries of CLCPs aligned by surface anchoring are usually 2D thin films, because the CLCPs are shaped in the rectangular LC cell, and the finite anchoring energies restrained the available thickness to a maximum value of ≈50 µm.[39]

Upon external stimuli (heat, light, solvent, electric, etc), the phase transition of CLCP is induced via the disruption of ordered mesogen alignment, which is further amplified into macroscopic deformation due to the interconnection between the mesogen alignment and the conformation of the polymer network. Figure 2e demonstrates the mechanism of thermal-responsive deformation, which is ascribed to the phase transition across the nematic-to-isotropic temperature (T_{NI}) by heating the LCPs.[23,40] The direct heating has been the most widely used methods to induce the phase transition, while the local heating based on photothermal effect has also attracted growing attentions due to the precise and remote control of light.[41–43] Figure 2f shows another commonly observed mechanism of typical athermal light-induced deformation, where the photochemical phase transition is triggered by the *trans-cis* isomerization of photochromic mesogens, such as the azobenzene moieties.[24,44,45] Due to the limited penetration depth of light, only the surface area effectively contracts or expands while the bulk of the LCPs remains unchanged.[46] Accordingly, the LCP film reversibly bends and unbends upon light irradiation with different wavelength, attributed to the non-uniform strain along the thickness.

3. Alignment Regulation toward LCP Actuators

Although monodomain CLCP sheets allow reversible and anisotropic stimuli-responsive deformations, their capabilities remain confined to simple shape changes, falling short of replicating the sophisticated bio-inspired movements required for practical applications. Hence, continuous efforts have been made to increase the designability of both the mesogen alignment and macroscopic structure for the achievement of more complex actuations. The developed alignment methods each exhibit distinct advantages on the designability of alignment and structure. Therefore, this section introduces the representative actuators categorized by the alignment methods.

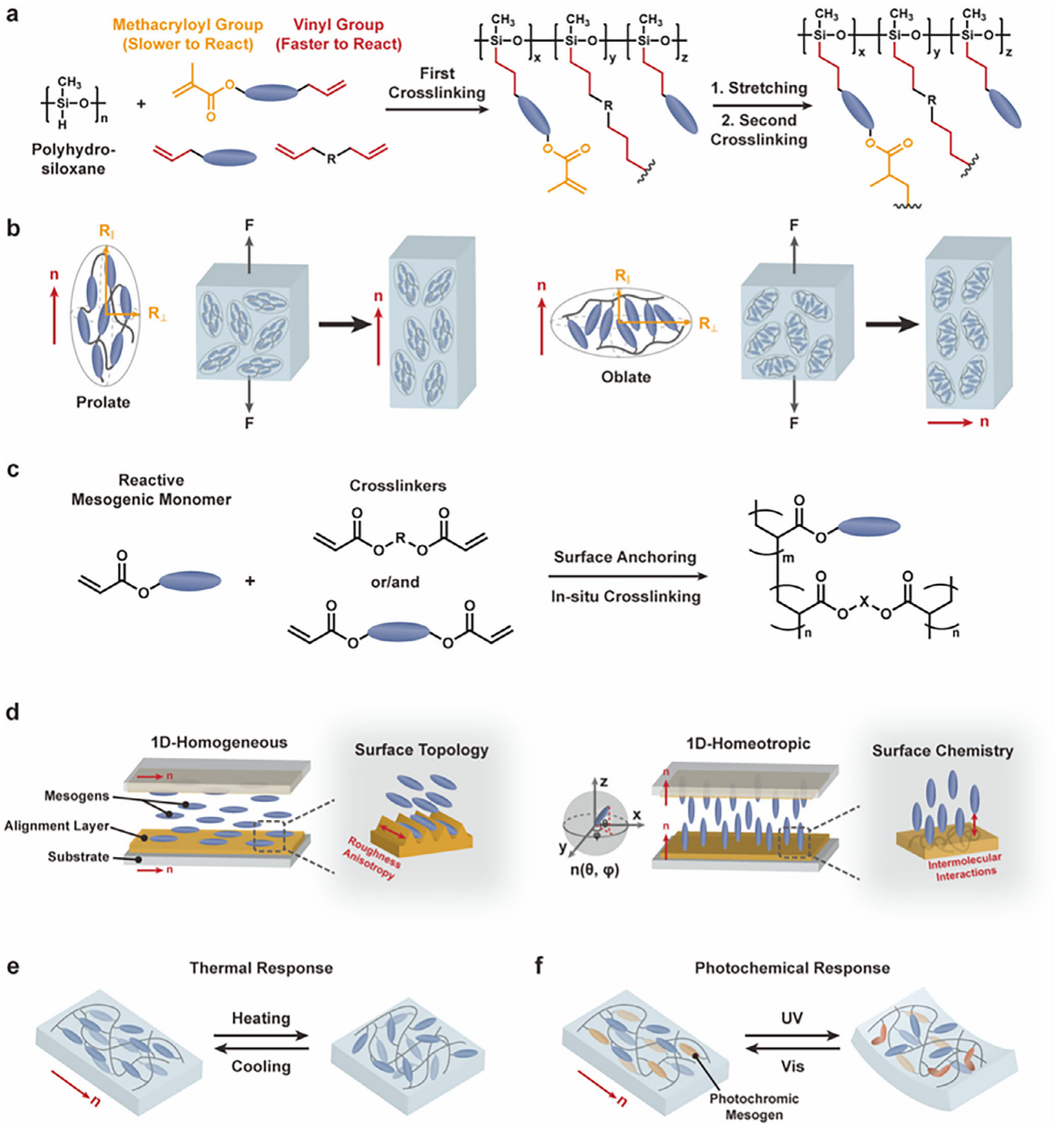

Figure 2. Material chemistries, alignment methods, and mechanisms of deformations for monodomain CLCP films. a) Two-step hydrosilylation reaction for the synthesis of the polysiloxane-based side-chain CLCPs. The blue rods represent mesogens, and the gray lines represent the polymer chains. b) Schematic illustration of the prolate ($R_{\parallel} > R_{\perp}$) and oblate ($R_{\parallel} < R_{\perp}$) local domains, with the demonstration of their alignment process upon uniaxial stretching. $R_{\parallel}$ is the radius of gyration parallel to the mesogen director while $R_{\perp}$ is the radius vertical to the director. The mesogen director is indicated by the red arrow *n*. c) Synthetic approaches to prepare the acrylate CLCPs via free radical polymerization from low-viscosity starting precursor. d) Alignment layers with planar microgrooves induce homogeneous alignment in the liquid crystal cell, while alignment layers with low polarity component induce homeotropic mesogen alignment. The director of mesogens is further manifested by the azimuthal angle (φ) and zenithal angle (θ). e) Thermal-responsive contraction-expansion deformation of monodomain CLCPs. f) Photochemical-responsive bending-unbending deformation, with the orange rods representing the *trans* isomers and the red bent-structures representing the *cis* isomers of azobenzene mesogens.

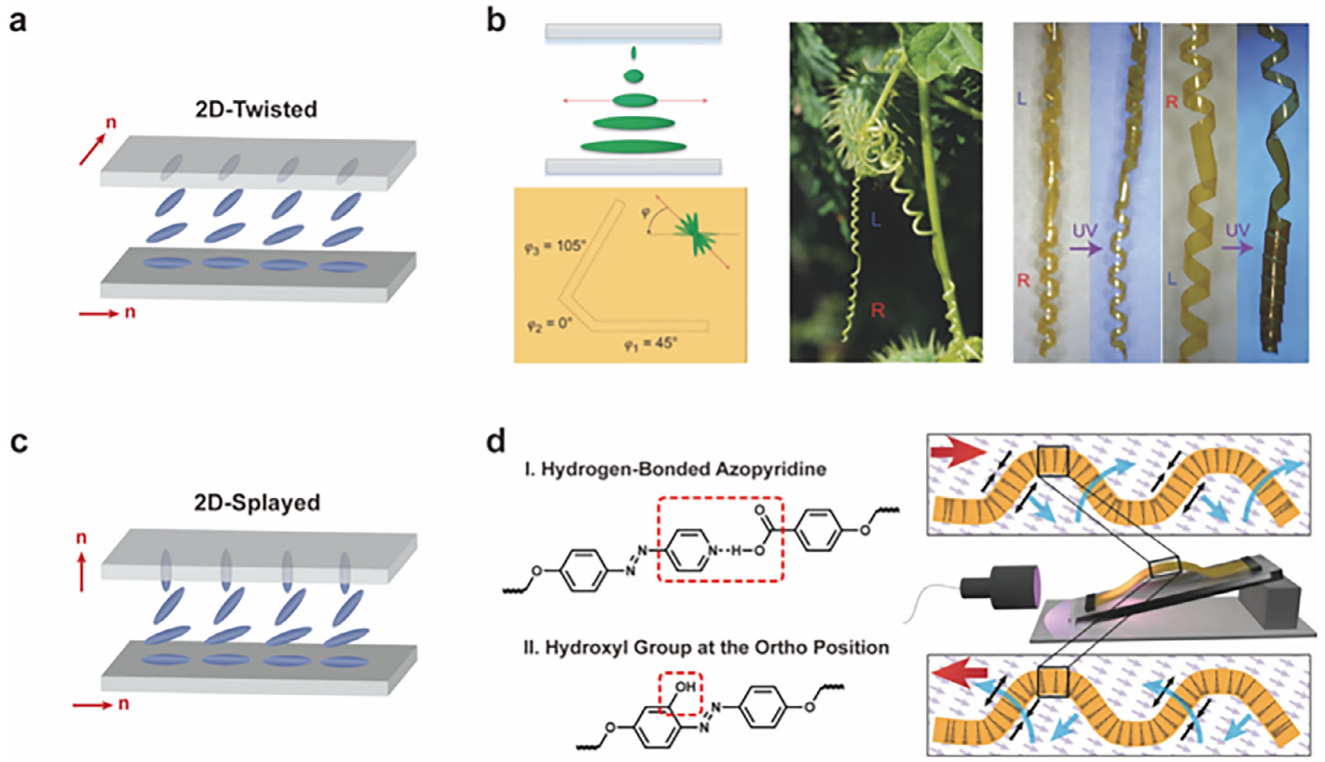

Figure 3. Nature-inspired LCP actuators featuring 2D director orientations. a) Schematic of the twisted alignment between two homogeneous alignment layers with mutually orthogonal anchoring orientations. b) A cucumber tendril-like actuator obtained by cutting a twist-aligned CLCP film. The angular offset (φ) characterizes the angle between the director of the mesogens at mid-plane and the cutting direction, and the dotted line represents the cutting direction of the ribbon. Reproduced with permission.[52] Copyright 2014, Springer Nature. c) Schematic of splayed alignment between a homogeneous and a homeotropic alignment layer. d) Chemical structures of two azobenzene derivatives with fast thermal relaxation, and the schematic illustration of the snake-like wave propagation achieved by a constrained splay-aligned CLCP film. The purple arrows indicate the irradiation direction of the UV light, the black ones show the contraction and expansion occurs on opposite sides of the film, the blue ones show the overall deformation of the film, and the red ones indicate the propagation direction of the wave. Reproduced with permission.[57] Copyright 2017, Springer Nature.

3.1. Surface-Enforced Alignment Toward LCP Actuators

Much efforts have been devoted to diversify the director orientations (from 1D to 3D) since Broer et al. applied surface-enforced alignment to the preparation of CLCPs.[31] Homogeneous and homeotropic alignment (1D) is easily obtained with symmetric alignment layers, while the twisted and splayed alignment (2D) were achieved by asymmetric alignment layers.[47,48] Specially, the introduction of chiral dopants enables the twisted alignment even with symmetric alignment layers.[49]

Figure 3a shows the twisted alignment (2D) where the azimuthal angle of mesogens gradually changes along the z axis.[50–52] Katsonis et al. made a twist-aligned photoresponsive CLCP film, and obtained a cucumber tendril-like ribbon by cutting the film according to the route shown in Figure 3b.[52] The angular offset φ_1, φ_2, and φ_3 respectively led to left-handed helices, achiral kink for connection and right-handed helices. The mixed-helicity spring exhibited simultaneous winding and unwinding in different helices upon UV irradiation, just like the natural cucumber tendril that find a support and lift a plant upward to the sun. Figure 3c demonstrates the splayed alignment (2D) features changing the zenith angle of mesogens, which facilitates the large-amplitude bending of CLCP films.[53–56] Broer et al. achieved continuous and directional snake-like waves under constant light illumination with a splay-aligned CLCP film (Figure 3d).[57] Azobenzene derivatives with hydrogen bonds or hydroxyl groups were incorporated to accelerate the cis-to-trans thermal relaxation of CLCPs, which contributed to the instantaneous bending and relaxation of the film once the UV light was applied and removed. A buckled initial shape was created to construct local exposed areas, where the left of the bump was irradiated while the right part was shadowed due to the self-shadowing effect of this light-absorbing film. Local curvature was induced in the exposed area attributed to the asymmetric photodeformation, which pushed the crest of the bump to move directionally. Notably, the displacement of the crest also changed the exposed areas of the film and induced a new curvature, thus constructing a feedback loop between the dynamically varied location of the bump and the exposed areas. Accordingly, the snake-like wave was achieved under constant light illumination due to the continuous propagation and regeneration of the bump. The use of splayed alignment gave an extra control to the direction of mechanical wave: the induced wave propagated away from the light source when the planar side was placed upward, while propagated toward the light source when the homeotropic side was up.

Patterned alignment layers were developed to construct more complex director orientations. Generally, the patterned alignment layers were made by photoalignment or

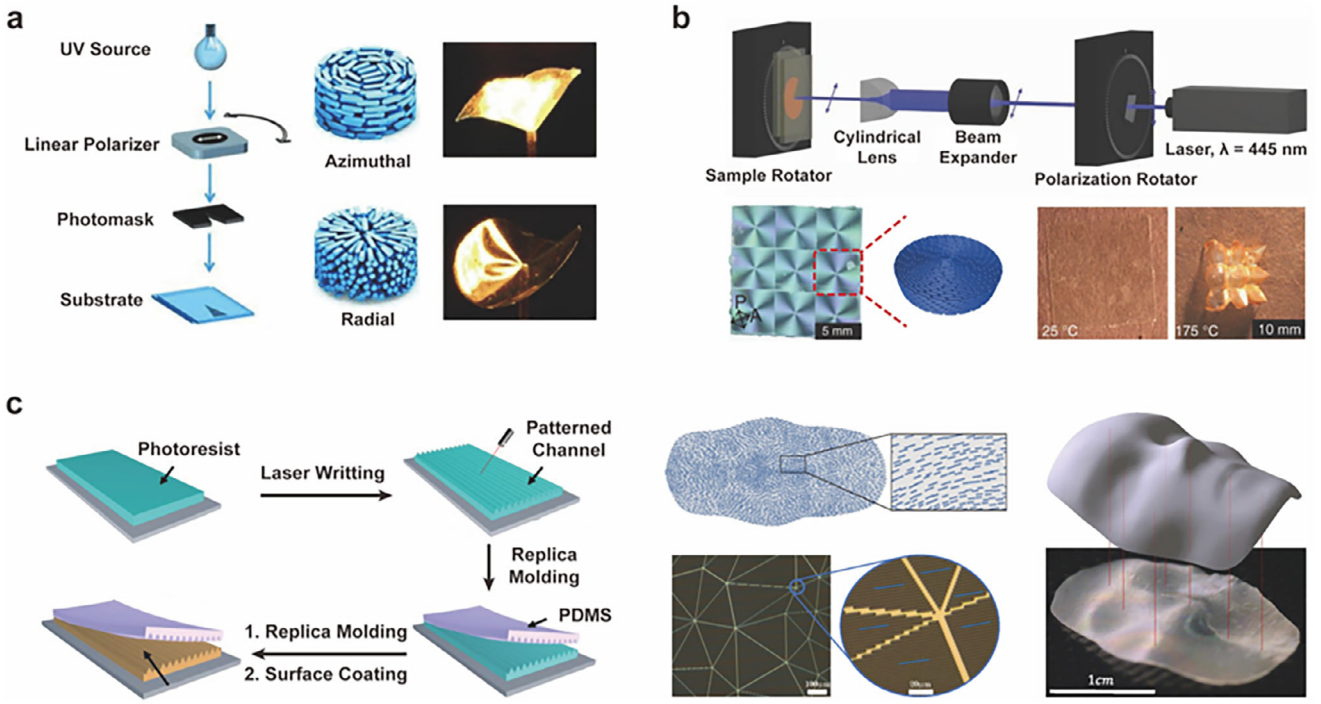

Figure 4. Nature-inspired LCP actuators featuring 3D director orientations. a) The typical setup of photoalignment and the actuation of CLCP films with azimuthal and radial alignments. Reproduced with permission.[62] Copyright 2012, Wiley-VCH. b) The improved setup of photoalignment for higher precision, with the demonstration of the complex topographic transformation achieved by the obtained voxelated CLCP film. Reproduced with permission.[63,64] Copyright 2013, Wiley-VCH; Copyright 2015, American Association for the Advancement of Science (AAAS). c) The process of fabricating alignment layers with patterned microgrooves through direct laser writing and replica molding. The director field is segmented into a triangulated mesh and designed by a numerical algorithm. The mesogen director in each triangular domain is precisely achieved in the CLCP film by patterned microgrooves. Upon heating, the film takes the shape of a face. Reproduced with permission.[65] Copyright 2018, National Academy of Sciences.

micromanufacturing.[58–61] Broer et al. presented a photomask-dependent photoalignment strategy to pattern the polymer chains in the alignment layers by tuning the angle between the wedge-shaped opening of the photomask and the polarization direction of light (**Figure 4a**).[62] The azimuthal and radial alignment patterns of polymer chains were achieved, and then replicated to the mesogen alignments via surface anchoring. The CLCP film with azimuthal alignment adapted the shape of a cone when heating, while the film with radial alignment showed a saddle shape.

Subsequently, White et al. enhanced the precision of photoalignment through the improved optical patterning setup. The sharp laser line (< 50 μm width, 1.6 cm length) and the point-by-point exposure system were used to achieve the precise control of alignment over an area of 0.01 mm^2 (Figure 4b).[63] Even more accurate control in a local volume as small as 0.0005 mm^3 was available through additionally enhanced light sensitivity of the mesogenic precursors.[64] A voxelated CLCP film containing nine +1 defects in a square array was obtained, which took a shape of nine cones upon heating due to the azimuthal contraction and radial expansion around each defect center.

Despite the high efficiency, the photoalignment constrained the choices of materials for alignment layers, which hinders the regulation of zenith angle due to its dependency on the polarity component of layers. To solve this problem, Yang et al proposed a strategy to regulate both the azimuthal and zenith angle for exquisite 3D director orientations via the combination of micromanufacturing and replica molding.[65] The patterned microgrooves were engraved on a rigid mold by direct light writing first, and transferred to the alignment layers by replica molding (Figure 4c). The microgrooves with a feature size of 1 μm provided high anchoring strength to guide the azimuthal angle, while the alignment material was chosen according to the desired polarity component to tune the zenith angle. These alignment layers ensured 3D director orientations with sub-10-micron accuracy, and oxygen-mediated thiol-acrylate "'click"' reaction was adopted to prevent nonuniform crosslinking density across the film. Accordingly, both the region-specific alignments and the magnitude of local principal strains of the film allowed to be precisely regulated, which took an intricate face-like shape upon heating as predicted by numerical algorithm.

Apart from the pursuit to the complexity of alignments, efforts have been also made to obtain aligned CLCP films with larger thickness for stronger force output and work capacity.[66–69] White et al. presented a facile approach to create thicker CLCP films by lamination (**Figure 5a**).[66] The orientation of individual CLCP films was patterned by photoalignment, and the reactive precursor of the CLCP films acted as the adhesive to bond adjacent films. The director orientation in the adhesive layer replicated the alignment of adjacent CLCP films, therefore the consistency of orientation was kept throughout the laminated films. The thickness of CLCP laminates reached 210 μm with this method, which

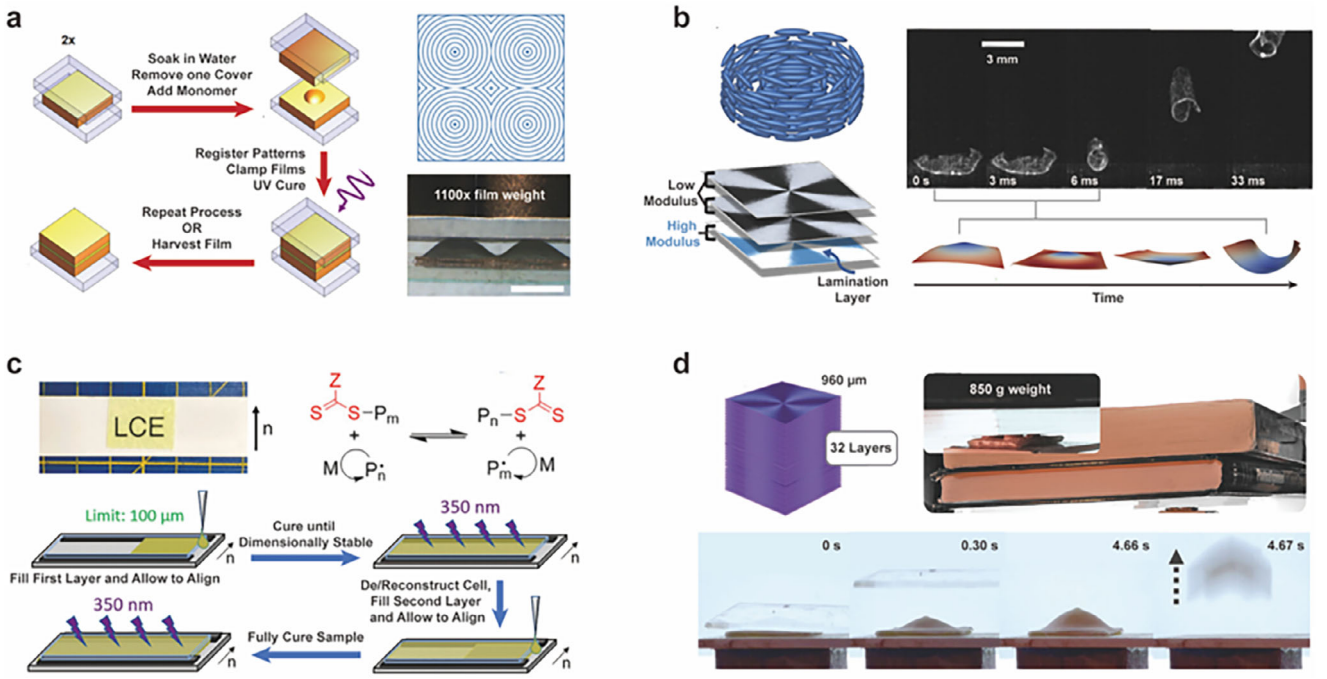

Figure 5. Strategies to increase the thickness of CLCP film aligned by surface-enforced alignment. a) The process to prepare thicker CLCP films via lamination. The alignment patterns and the bearing capacity of a four-layered CLCP laminate. Reproduced with permission under the CC BY 4.0 license.[66] Copyright 2018, The Authors, published by Springer Nature. b) A three-layered CLCP laminate prepared by stacking a high-modulus patterned film and two low-modulus ones, with the experimental results and schematic illustration of the rapid jumping locomotion achieved by the laminate on a hot plate. Reproduced with permission under the CC BY 4.0 license.[67] Copyright 2023, The Authors, published by AAAS. c) Mechanism of PET-RAFT polymerization and the process to prepare thicker CLCP films via PET-RAFT. Reproduced with permission under the CC BY 4.0 license.[68] Copyright 2024, The Authors, published by American Chemical Society (ACS). d) Schematic of a 32-layered CLCP film embedded with +1 topological defect, with the images showing its loading capacity and the leaping process. Reproduced with permission.[69] Copyright 2023, Wiley-VCH.

lifted over 1100 times the weight of the film itself. They further laminated two softer 30-µm CLCP films and a stiffer 30-µm CLCP film into a 90-µm film, with identical alignment pattern of +1 topological defect embedded (Figure 5b).[67] When the stiffer side was placed on a hot surface, only the bottom layer was heated initially, and the film deformed upward into a cone. Subsequently, the heat was transferred to the upper layers. The mismatch of strain between the stiffer layer and the softer layers was created since the softer layers contracted much faster than the stiffer one, which tended to bias the curvature in the opposite direction. Notably, the conical shape lacked smooth deformation pathways between the up and down alignments. The initial upward alignment was locked in with an energy barrier, thus contributing to the accumulation and storage of the strain energy. As a result, the snap-through occurred once there was a sufficient inverting spontaneous curvature. The stored energy was released instantaneously, causing the laminated film to jump to a height over 200 times its own thickness.

In order to reduce the detachment caused by additional adhesives, Gleeson et al. proposed a new chemical bonding strategy and achieved LCP films with thickness up to 250–300 µm.[68] The photoinduced electron/energy transfer reversible addition-fragmentation chain transfer (PET-RAFT) polymerization was used for crosslinking, whose extent of reaction was easy to control due to its stop-start characteristic (Figure 5c). The previous layer was partially cured until dimensionally stable, with the residual unreacted monomers served as the adhesive to chemically bond the next layer. Also utilizing a chemical bonding strategy, White et al. designed an LCE that exhibited adhesive properties when exposed to water, and achieved a 32-layered film (thickness ≈ 1 mm) through direct lamination in water.[69] The +1 topological defect was built in the alignment pattern of this thick film, which took a conical shape upon heating and demonstrated a considerable load-bearing capability of up to 850 g (Figure 5d). The actuated film was first constrained in a domed shape under load, contributing to the accumulation and storage of strain energy. The film with a transient pseudo-bistable state exhibited snap-through behavior upon load removal, rapidly reverting to its initial conical shape and triggering a leaping motion due to the instantaneous release of strain energy.

The surface-enforced alignment frustrates in applications that require complex 3D functional structures, since it usually restrained the geometry of CLCPs in simple 2D films. Nevertheless, it still holds a unique advantage in the preparation of CLCPs featuring patterned alignment, especially for the alignment with through-thickness variation.

3.2. Field-Assisted Alignment toward LCP Actuators

Field-assisted alignment generally indicates the regulation of mesogen alignment under an electric field or magnetic field,

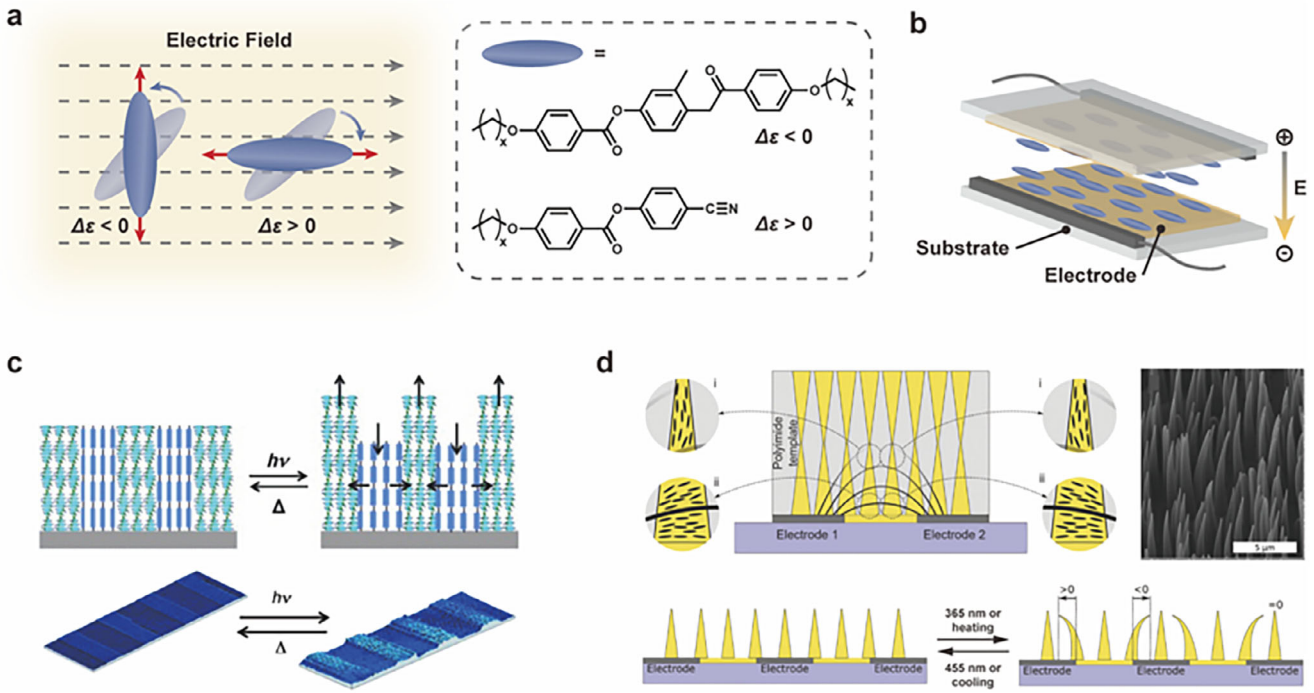

Figure 6. Mechanisms of electric field-assisted alignment and the actuators obtained accordingly. a) Molecular structures of the mesogens compatible with electric field-assisted alignment, and $\Delta\varepsilon$ is the anisotropy of the dielectric susceptibility for the mesogen. b) The typical setup for electric field-assisted alignment that induces homogeneous alignment. c) A CLCP strip with alternating twisted and homeotropic alignment, which demonstrates dynamic changes of surface topology upon UV irradiation. Reproduced with permission.[84] Copyright 2012, Wiley-VCH. d) The region-specific alignment near the top and bottom of the CLCP cilia, the scanning electron microscope (SEM) image of cilia, and the demonstration of their collective motion upon heat or light. Reproduced with permission under the CC BY 4.0 license.[85] Copyright 2022, Eindhoven University of Technology, published by Wiley-VCH.

depending on the dielectric or diamagnetic anisotropy of mesogens. Low-viscosity mesogenic precursors are preferred by field-assisted alignment since they allow efficient alignment with broadly accessible field strength, while ultra-high field strength is required to align high-viscosity precursors.[70–73] The field-assisted alignment also enables director orientations from 1D to 3D patterns similar to the surface-enforced alignment, and additionally facilitates the fabrication of microarrays beyond 2D films through the combination of replica molding.

3.2.1. Electric Field-Assisted Alignment toward LCP Actuators

The electric field-assisted alignment has been prevalently applied to liquid crystal display already, and was further expanded into the preparation of aligned CLCPs in 1990s.[74–76] The direction of the electric field and the dielectric anisotropy of mesogens determine the alignment of mesogens upon electric field (**Figure 6a**).[77–79] The widely-used diacrylate mesogens commonly possess negative dielectric anisotropy ($\Delta\varepsilon < 0$) and are aligned vertical to the direction of electric field,[80] while the mesogens with polar groups, such as nitriles or esters, exhibit positive dielectric anisotropy ($\Delta\varepsilon > 0$) and are aligned parallel to the direction of electric field.[81,82] The average dielectric anisotropy of mesogenic precursors is tunable from negative to positive according to the proportion of mesogenic monomers with distinct polarities.[79] Figure 6b demonstrates a typical setup for electric field-assisted alignment, where the mesogenic precursors are aligned upon the electric field generated by the two electrodes. In most cases, the electric field-assisted alignment is used along with surface-enforced alignment, with the parallel-plate electrodes sandwiched between glass substrates and alignment layers.[76,83]

To achieve complex alignment, Broer et al. designed stripe-patterned electrodes coated with planar alignment layers (Figure 6c).[84] The chiral mesogenic precursor with positive dielectric anisotropy exhibited homeotropic alignment upon local electric fields, while other regions remained the twisted alignment. Dynamic surface topology of the CLCP strip was achieved, where the twist-aligned regions bulged upon UV irradiation while the homeotropic-aligned regions dented. Later on, they designed interdigitated electrodes coated with planar alignment layers and achieved splayed alignment in CLCP cilia with the combination of a track-etched template (Figure 6d).[85] The mesogens near the tapered pores aligned parallel to their long axis due to the confinement effect, while the mesogens near the electrodes aligned parallel to the in-plane electric field. CLCP cilia with dense surface coverage were shaped in the well-defined template, which demonstrated collective motion upon heat or light.

3.2.2. Magnetic Field-Assisted Alignment toward LCP Actuators

The mechanism of magnetic field-assisted alignment is quite analogous to the electric field-assisted counterpart.[86] Generally, the mesogens with aromatic rings exhibit positive diamagnetic

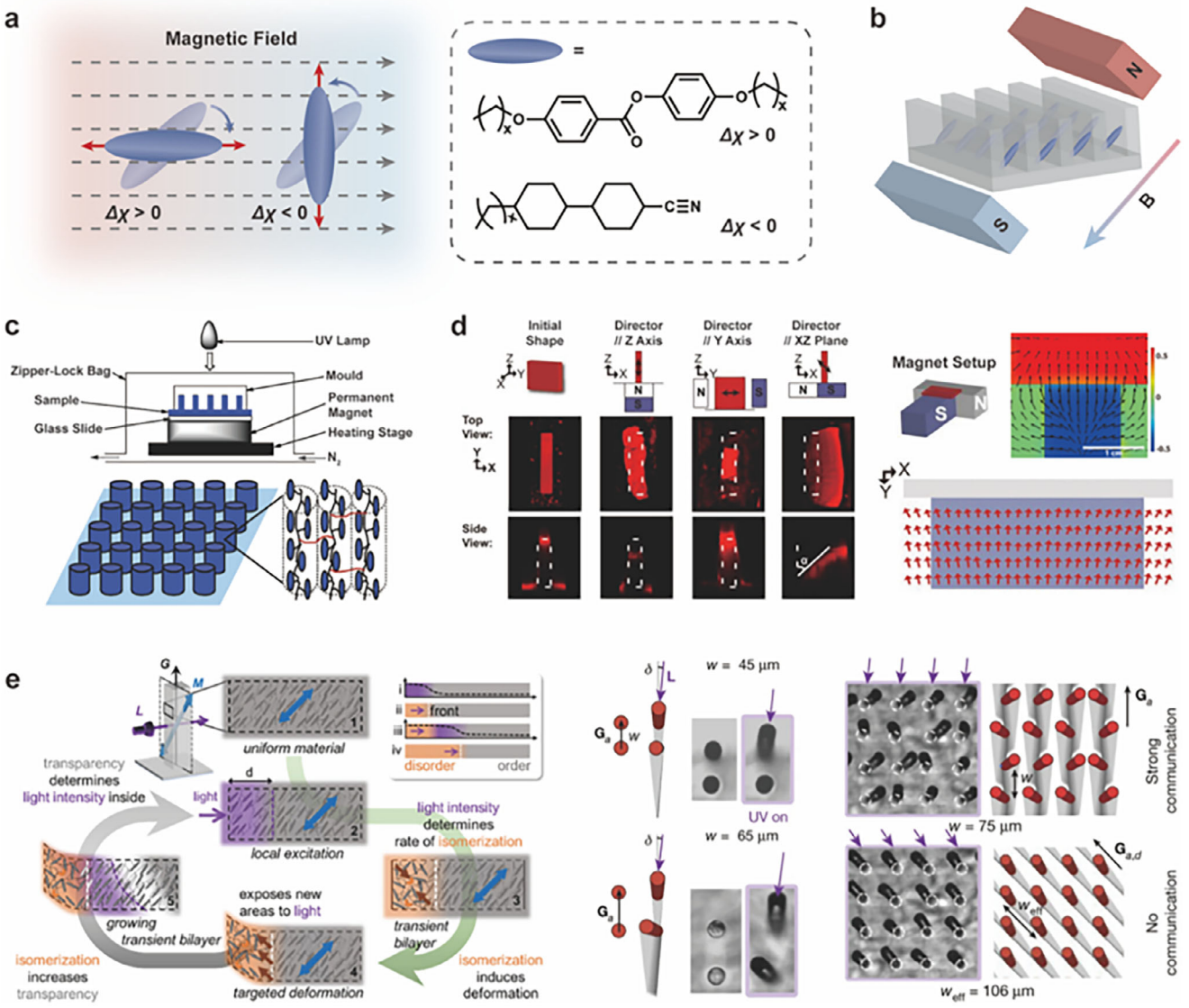

Figure 7. Mechanisms of magnetic field-assisted alignment and the actuators obtained accordingly. a) Molecular structures of the mesogens compatible with magnetic field-assisted alignment, and $\Delta\chi$ is the anisotropy of the diamagnetic susceptibility for the mesogen. b) The typical setup of magnetic field-assisted alignment that induces tilting alignment. c) The setup to prepare an array of micropillars with homeotropic alignment in each pillar. Reproduced with permission.[90] Copyright 2006, ACS. d) Single CLCP microplates that demonstrate different types of deformation, with the directors of their uniaxial alignment indicated by double-handed black arrows. The photos below show their original shape and the deformed shapes. Under a patterned magnetic field generated by the T-shaped magnetic setup, region-specific uniaxial alignment is achieved in the array of CLCP microplates, with the simulation result of the patterned magnetic field demonstrated. The array shows spatially continuous tilting upon heating, with the red arrows representing the direction and magnitude of the tilting. Reproduced with permission under the CC BY 4.0 license.[95] Copyright 2018, The Authors, published by the National Academy of Sciences. e) Illustration of the underlying opto-chemo-mechanical feedback in an CLCP micropillar with noncollinear geometric axis (G), mesogen alignment (M), and light direction (L). In the array of micropillars, the string direction of two adjacent micropillars and their interpillar distance serve as another symmetry axis (Ga). Cooperative movement across the array is achieved by regulating the directional misalignment between Ga and L. Reproduced with permission.[97] Copyright 2022, Springer Nature.

anisotropy ($\Delta\chi > 0$) and are aligned parallel to the direction of the magnetic field,[87,88] while the mesogens with cyclohexyl rings exhibit negative diamagnetic anisotropy ($\Delta\chi < 0$) and are aligned vertical to the direction of magnetic field (**Figure** 7a).[89]

The combination of magnetic field-assisted alignment and replica molding provides an efficient way to construct aligned CLCP microarrays (Figure 7b),[90–95] which was first exploited by Keller et al. They fabricated an array of micropillars with axial alignment that reversibly contracted in response to a small change of temperature (Figure 7c).[90,91] Subsequently, region-specific alignment over single microfeatures was achieved through the construction of a patterned magnetic field.[96] Aizenberg et al. utilized a T-shaped magnet setup to build spatially distinguished uniaxial alignment in the individual microplates of

the CLCP microarray, which demonstrated region-specific direction of tilting upon heating (Figure 7d).[95]

They further utilized the magnetic field to align the mesogens oblique to the geometric axis of an array of photo-responsive micropillars, which achieved self-regulated cooperative motions featuring complex trajectories under a stationary light source through an igneous design of opto-chemo-mechanical feedback (Figure 7e).[97] The single photo-responsive micropillar was designed to possess three linearly independent symmetry axes, including the geometric axis (G), the mesogen alignment (M) and the direction of incident light (L). A transient bimorph was formed in the micropillar upon directional illumination of a stationary light source, where the order-to-disorder front dynamically propagated due to the photo-induced transparency. Notably, the order-to-disorder transition also transformed the geometric axis and exposed areas of the micropillar due to the accompanying alignment-dependent deformation, thus constructing a feedback loop between the evolving bimorph and the trajectory of motion. Another symmetry axis, Ga, was additionally incorporated in the feedback loop regarding the array of micropillars, which was defined by the string direction of two adjacent micropillars and their interpillar distance. With a slight directional misalignment between Ga and L, the single micropillar deformed out of the string direction, leading to asymmetric exposure of the adjacent micropillar and consequently a domino effect of self-sorting motions across the array.

3.3. Rheological Alignment toward LCP Actuators

The rheological behavior of commercial LCPs was widely-studied as early as the 1970s, mainly attributed to the research boom of aramid, which mainly focused on lyotropic systems due to their great backbone rigidity.[98–100] In 1998, Ugaz et al. have made significant progress toward the rheological behavior of thermotropic LCPs, which possessed more flexible backbones as the precursors for CLCP.[101] They confirmed that these thermotropic LCPs exhibited unique flow-alignment behavior, unlike the lyotropic LCPs whose mesogen directors were dominated by tumbling under shear flow. The recent popularity of direct ink writing (DIW) 3D printing has resurged the research interests on the rheological behavior of LCPs, and several works that detailly exanimated the rheological behavior of mesogenic oligomers/inks have been reported.[102,103]

Noticeable differences exist between rheological alignment and mechanical alignment, though they both establish on the force-induced alignment. First, the flowable precursors, such as the widely-used non-crosslinked oligomers, are preferred by rheological alignment,[104–106] while the stretchable precursors required by mechanical alignment exhibit poor flowability in solution or the melted state. Second, the rheological alignment of LCPs exhibits pronounced time-dependent characteristics and complex underlying physics due to the distortional elastic effect and polydomain nature of LCPs, while the mechanism of mechanical alignment is comparatively simple. Third, the mechanical alignment falls short of patterned programming of mesogens, while the rheological alignment provides an efficient way to pattern the alignment through the combination with DIW.

The rheological alignment generally includes the alignment under elongational flow, shear flow, or the mixed elongational-shear flow.[107–115] The pure elongational flow is observed in thermal-drawing or electrospinning, and the corresponding mechanism is similar to that of mechanical alignment.[108–110] As for the pure shear flow, it has been mainly used to investigate the rheology of LCPs rather than the fabrication of actuators.[98,113–115] To date, the extrusion has been the most commonly used processing method for the fabrication of LCP actuators that obey the mechanism of rheological alignment, where the mixed elongational-shear flow is responsible for the progressive alignment. The extrusion facilitates the continuous and stable production of aligned filaments/fibers within the submillimeter to millimeter range.[116,117] Moreover, its combination with additive manufacturing (DIW) further enables the convenient construction of actuators with diverse 3D geometries. The DIW was first applied to LCP actuators by Ware et al. and Sánchez-Somolinos et al. in 2017,[17,18] and has evoked wide attention from the breakthrough works done by Lewis et al.[19] The DIW pioneers in achieving predictable and designable motions of LCP actuators, since both their alignment and geometry allow to be consistently and precisely regulated in a digitally controled manner. This characteristic has promoted its popularity among materials chemists, physicists, and engineers recently, thus motivating the surge of interdisciplinary research for the considerations in soft robotics.

3.3.1. Actuators Aligned under Elongational Flow or Shear Flow

The thermotropic LCPs experience markedly different stress conditions in shear flow versus elongational flow,[118] leading to distinct differences in their rheological behavior (**Figure 8**). In elongational flow, the left side of the sample is fixed (velocity = 0), while the right side experiences the maximum stretching speed. Consequently, the direction of the velocity gradient aligns parallel to the flow direction. For a small fluid element (the cubic cell shown in Figure 8a), the stresses act perpendicular to the cell's right surface (δ_{xx}), which induce axial elongation of the cubic, and the alignment of microdomains along the flow direction. While nematic LCPs exhibit *flow alignment* of mesogens, smectic LCPs show perpendicular orientation of the smectic layers at low strain rates, transitioning to director alignment along the flow direction beyond a critical strain rate, associated with sliding between mesogens within the smectic layers.

For the shear flow in a pipe, the pseudoplastic LCPs exhibit a radial gradient of shear stress due to their inherent shear-thinning properties. Therefore, the higher τ near the pipe wall contributes to better mesogen alignment, while the low τ near the center results in less-oriented mesogens. It's worth noting that the shear-thinning behavior of LCPs is dominated by domain rearrangement attributed to their unique polydomain nature, which is distinct from the chain disentanglement mechanism widely accepted for isotropic polymers.

The rheological behavior of LCPs under shear flow becomes much more complicated than under elongational flow. The bottom surface of the sample exhibits zero velocity (assuming no slip), while the top surface moves at maximum velocity. Consequently, the direction of the velocity gradient is perpendicular to

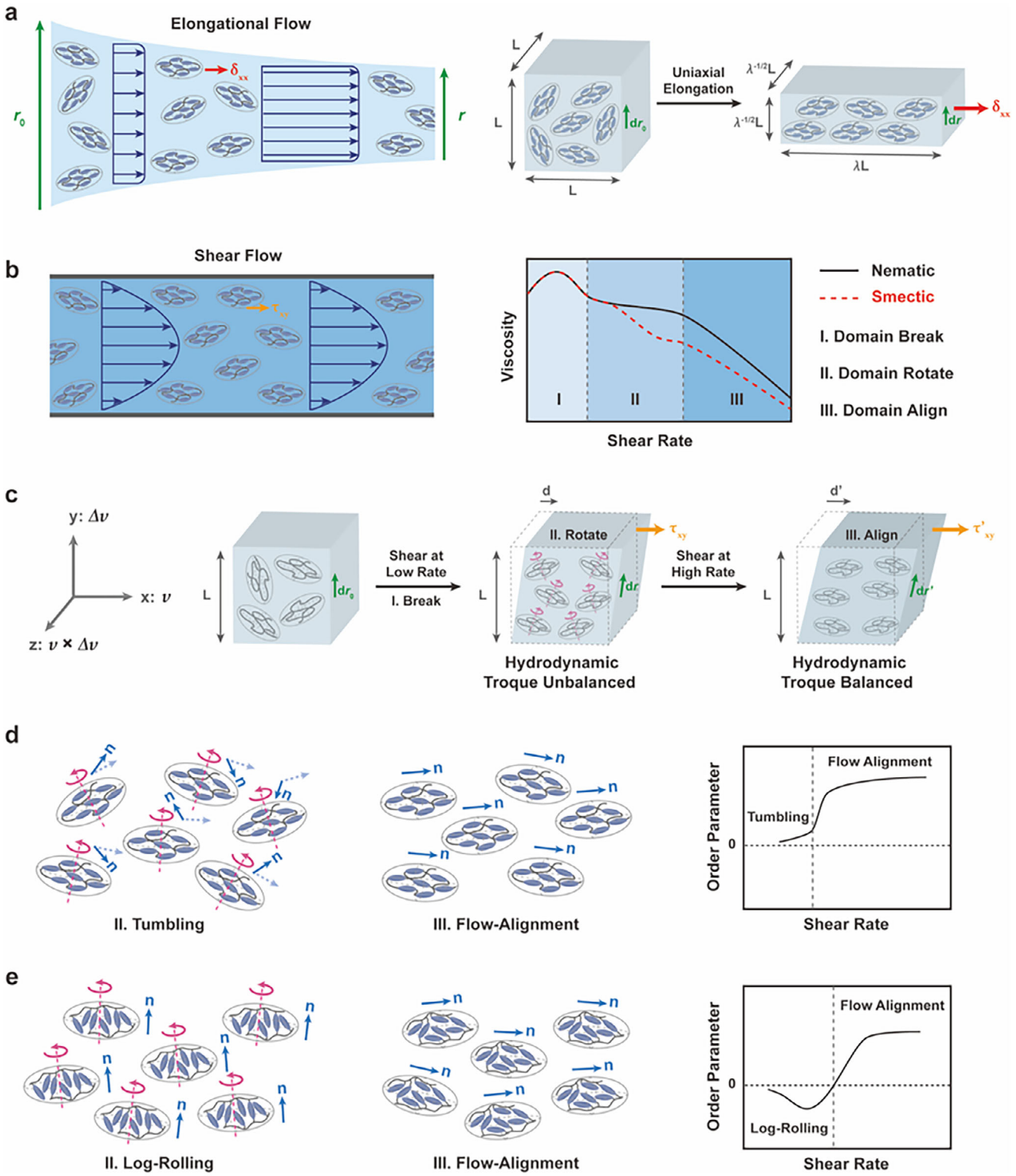

Figure 8. Alignment mechanisms and characteristics of LCPs under elongational and shear flows. a) The schematic illustrations of the alignment process under elongational flow. The length of the blue arrow represents the flow velocity magnitude, and the red arrow represents the tensile stress δ. The neighboring diagram depicts the mechanical response of a fluid element subjected to elongational flow. b) The schematic illustrations of the alignment process under shear flow, the yellow arrow represents the shear stress τ. The neighboring diagram shows the rheological behavior of nematic and smectic LCPs under shear flow. c) The mechanical response of a fluid element subjected to shear flow. d,e) Schematic of domain state evolution in d) nematic and e) smectic LCPs under shear flow. The director, defined as the local average mesogen orientation, is indicated by the blue arrow *n*; the right panel plots the order parameter versus shear rate.

the flow direction (Figure 8b,c). For a small fluid element (the cubic cell shown in Figure 8c), the stresses act on the top surface of the cell (τ_{xy}) and induce the hydrodynamic torque of the microdomains, which are partially responsible for the complicated rheological behavior featuring three distinct regimes (Figure 8b).

Upon the inception of shear flow, the microdomains break into smaller ones, concurrently triggering an apparent viscosity overshoot (Regime I). Subsequently, these domains continuously rotate since the hydrodynamic torques are unbalanced in this stage (Regime II), where the alignment behavior of nematic LCPs is distinct from that of smectic LCPs. The random rotation of prolate domains in nematic LCPs leads to *director tumbling*. Accordingly, a relatively steady viscosity and a tiny increase of order parameter are observed (Figure 8d). As for the smectic LCPs, the rotation of oblate domains contributes to the *log-rolling* alignment (the director aligns perpendicular to the flow direction) since the domain boundaries align along the flow direction,[119,120] leading to a decrease of viscosity and obvious increase of order parameter (Figure 8e). At high shear rates, domains align parallel to the flow direction as hydrodynamic torques equilibrate at the characteristic *Leslie angle* (Regime III). A sharp decrease of viscosity is observed in this *flow alignment* regime, accompanied by a noticeable increase of order parameter. Specially, the transition of LC phase is additionally observed for smectic LCPs.

Thermal drawing and electrospinning are typical methods for processing fine fibers, where the rheology of LCPs is often approximated as pure extensional flow due to the dominant role of elongational deformation during rapid thinning and the high surface-area-to-volume ratio of fine fibers. The fibers are drawn out from the melt of the polymers during thermal-drawing, and the accompanying elongational flow along the direction of drawing leads to axial mesogen alignment of the fibers.[108,121,122] Broer et al. prepared an array of photo-responsive LCP fibers by thermal-drawing, which performed concerted motion similar to the natural cilia upon UV light (**Figure 9**a).[121] The droplets of mesogenic oligomers were casted on a glass substrate in an array initially, followed by thermal-drawing and photo-crosslinking. Upon UV irradiation, the fibers with axial mesogen alignment simultaneously followed the light source in all directions. The cooperative motion was further utilized to transport floating objects by creating flows in the liquid environment. Electrospinning transforms the solution or melt of polymers into a fluid jet upon electric fields, which facilitates the fabrication of ultrafine fibers from the nanometer to micron scale and simultaneously induces elongational flow along the direction of jet for alignment.[123–125] Yu et al. prepared photo-responsive LCP nanofibers and subsequently processed them into mat via deposition, which featured superhydrophobicity due to the noticeable roughness of its surface (Figure 9b).[125] The surface of the mat exhibited reversible superhydrophobic adhesion upon alternated irradiation of UV–Vis light attributed to the variation of roughness, thus achieving the pinning and sliding of discrete water droplets at any desired position.

Though the shear flow is commonly observed in combination with elongation flow for alignment, several inspiring works that utilized the shear flow alone to endow LCP actuators with gradient alignment have also been reported.[104,115,126] For instance, Shepherd et al. built gradient alignment in a CLCP film through the combination of digital light processing (DLP) 3D printing and shear flow-induced alignment.[126] The resin tray was rotated cyclically to induce the shear flow for gradient alignment, and the aligned mesogenic oligomers were cured by digital light source in a layer-by-layer manner (Figure 9c). The resulted CLCP film bent upon heating and further achieved quadruped-like crawling on a corrugated substrate by localized heating.

3.3.2. Actuators Aligned under Mixed Elongational-Shear Flow

The application of 3D printing largely facilitates the fabrication of LCP actuators that require customizable material properties and complex architectures. Among various 3D printing techniques, the DIW has been most extensively investigated since it further ensures the regulation of mesogen alignment via extrusion beyond the construction of 3D structures.

Figure 10a shows the chain extension chemistry for the preparation of mesogenic inks used in DIW, which are typically the non-crosslinked flowable oligomers. The reactive mesogenic monomers and thiol/amine chain extenders are utilized to synthesize the oligomers via thermal-induced thiol/aza-Michael addition.[15,16] The oligomers are aligned by extrusion under the mixed elongational-shear flow, with the alignment fixed by subsequently applied photocrosslinking. This newly developed materials chemistry offers a facile and broadly accessible way for researchers to synthesize CLCPs, and the commercialized production of polymerizable mesogenic monomers has further simplified the synthesis.

Figure 10b demonstrates the extrusion-induced alignment of nematic oligomers under mixed elongational-shear flow.[116,117] The polydomain oligomer initially undergoes elongation flow when passing through a cylindrical nozzle, and the shear flow gradually spreads inward from both ends as the flow progresses. The mixed flow eventually aligns both the polymer chains and mesogens along the flow direction, with better alignment achieved near the inner wall of the nozzle.[103] Therefore, the extruded LCP filaments during DIW printing show a core-shell structure, with better mesogen alignment built in the shell (Figure 10c).[127,128] These filaments are deposited on the platform according to the predesigned paths by shifting the nozzle in *X*-*Y* plane, and is cured by photo-crosslinking after one layer is printed. The next layer is deposited on the previously cured layer after the *Z*-axis shift of the platform, and 3D actuators are finally obtained through the layer-by-layer printing.[20,129]

The single extruded CLCP filament performs contractile-expansive deformation along the axis upon stimuli, because the mesogen alignment is axially symmetric despite the gradient. Patterned alignment is further achieved by simply regulating the printing paths, since they are in accordance with the axis of the deposited filaments. **Figure 11** shows several typical printing patterns, along with their corresponding actuation modes demonstrated.[17,19,130] The uniaxial printing path leads to the linear contraction of the printed one-layered CLCP film (Figure 11a), while the azimuthal path enables the shape transformation from a flat sheet to a cone (Figure 11b). Twisting and bending are achieved with bilayer CLCP films, where the printing path of the top layer is perpendicular to that of the bottom layer (Figure 11c).

Numerous bionic LCP actuators have been created by DIW. Chen et al. printed a flower-shaped bilayer CLCP film.[131] The

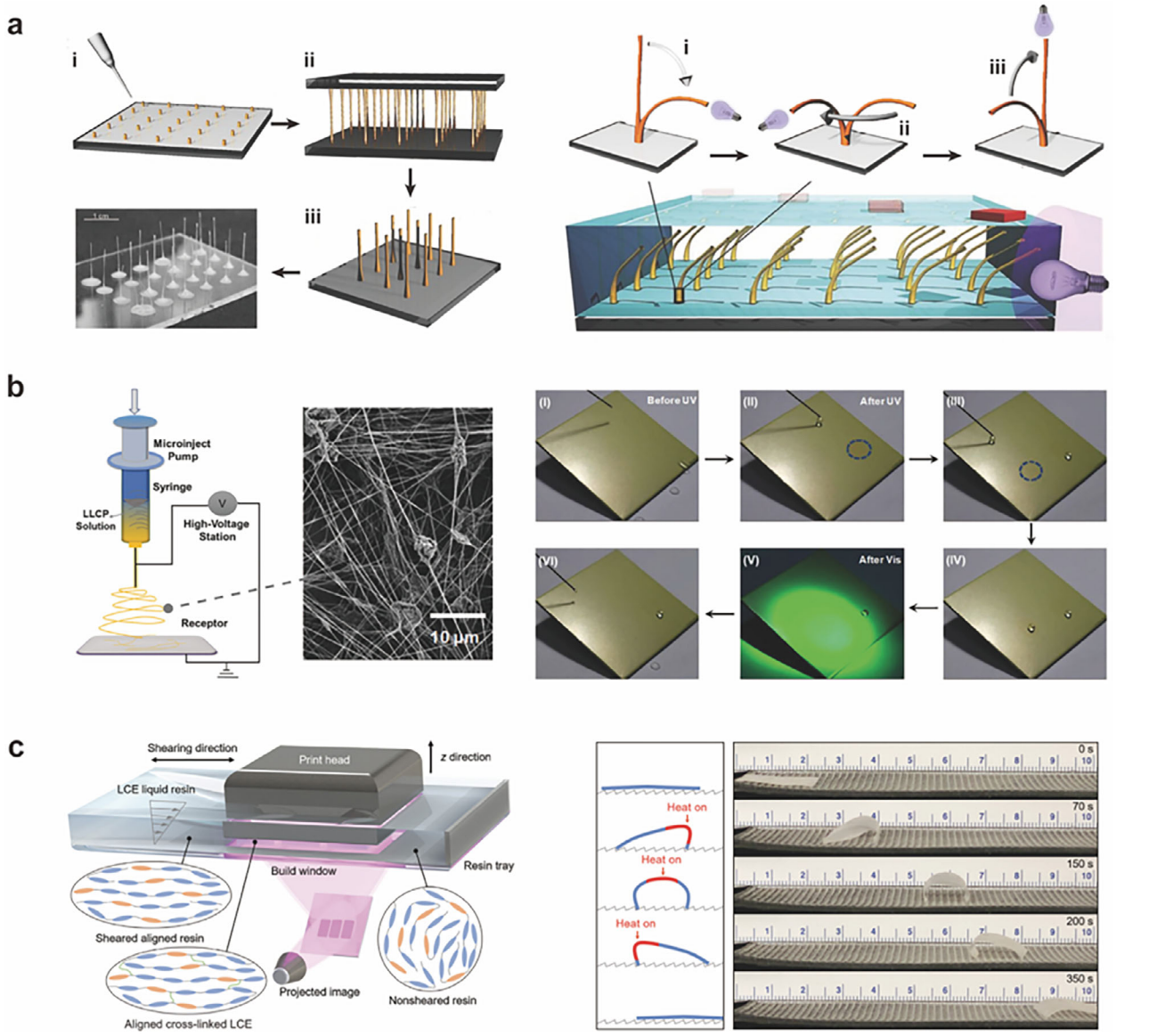

Figure 9. LCP actuators are aligned under pure elongational flow or shear flow. a) An array of photo-responsive CLCP fibers fabricated through: i) casting, ii) thermal drawing, and iii) photo-crosslinking. Demonstrations of the light-tracking behavior of a single fiber and an array of fibers. The collective bending of the array creates flows and transports floating objects. Reproduced with permission under the CC BY 4.0 license.[121] Copyright 2016, The Authors, published by Wiley-VCH. b) A schematic depiction of the electrospinning setup and the SEM image of the mat obtained by depositing the nanofibers. The photographs show photo-steerable pinning and releasing of water droplets on the superhydrophobic mat: i) water droplets roll smoothly on the mat, ii-iv) the droplets are pinned at the UV-irradiated circular areas; v, vi) the mat releases a pinned droplet after visible light irradiation. Reproduced with permission.[125] Copyright 2019, Wiley-VCH. c) A setup that prints aligned CLCP film under shear flow, with schematic illustration and experimental results of the quadruped-like crawling of the printed film. Reproduced with permission under the CC BY 4.0 license.[126] Copyright 2021, The Authors, published by AAAS.

top and bottom layers were printed at 45°/135° with respect to the long axis of the pedal, which coiled similar to the helical closure of a flower upon UV light (**Figure** 12a). The authors subsequently assembled a hybrid butterfly-like actuator with printed CLCP wings and a passive main body, where the wings flipped like the movement of a natural butterfly under UV light. Multimodal actuations were further achieved through hybrid design and selective manipulation of active CLCP components. Zhao et al. assembled three printed CLCP fibers and a silicone rod into an elephant trunk-like cylindrical actuator, where the straightly arranged CLCP fiber acted as the longitudinal muscle and the helically arranged CLCP fibers served as oblique muscles (Figure 12b).[132] The selective actuation of CLCP fibers drove the passive deformation of the silicone rod in different modes, and dexterous motion similar to an actual elephant trunk was achieved through multi-step actuation of the fibers due to the continuous switch of deformation modes. More refined structures of the printed actuators were realized through the

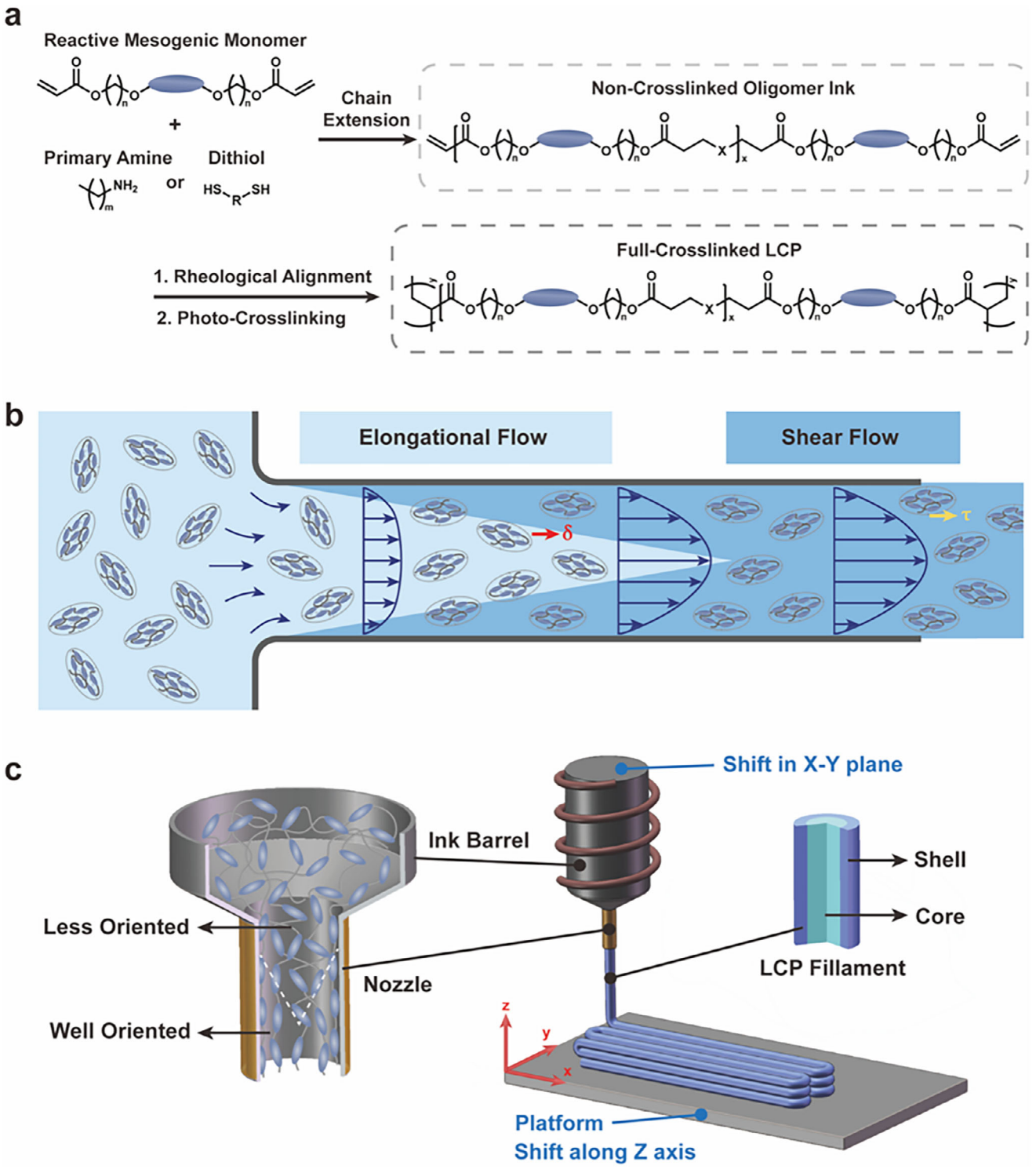

Figure 10. Material chemistry, mechanism of alignment, and illustration of additive manufacturing for LCP actuators printed by direct ink writing (DIW). a) Schematic of chain extension chemistry for the synthesis of mesogenic inks. b) Mechanism of alignment under mixed elongational-shear flow during extrusion. c) Schematic illustration of the printing process of DIW. The extruded CLCP filaments are aligned under mixed flow and exhibit a core-shell structure. The filaments are deposited in a layer-wise manner to construct 3D geometries.

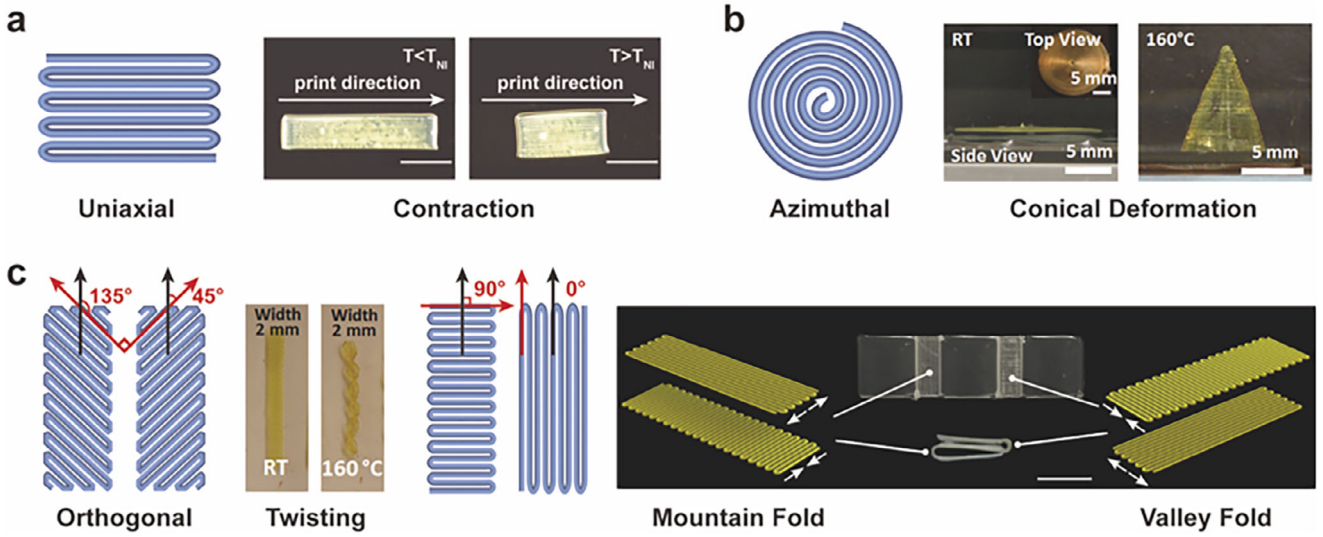

Figure 11. Common printing patterns and their corresponding actuation modes. a) Schematic of uniaxial printing path and images of a uniaxially printed CLCP film that contracts upon heating. Reproduced with permission.[19] Copyright 2018, Wiley-VCH. b) Schematic of an azimuthal printing path and images of a disk-shaped film that takes a conical shape upon heating. Reproduced with permission.[17] Copyright 2017, ACS. c) Schematic of mutually orthogonal printing paths built in the two-layered CLCP film. The two-layered film twists upon heating when the top and bottom layers are printed at 45°/135° with respect to the long axis. The film printed at 0°/90° bends into a mountain fold, while the film printed at 90°/0° bends into a valley fold. The red arrows indicate the printing paths, while the black arrows indicate the long axis of the printed film. Reproduced with permission.[17,130] Copyright 2017, ACS. Copyright 2019, AAAS.

incorporation of an electric field, since much slenderer filaments with diameters from 4.5 to 60 μm were available under electric field force while the diameter of commonly observed filaments exceeds 100 μm (Figure 12c).[133] With this strategy, Lu et al. printed an array of microgrippers along a sinusoidal path, which alternatively closed and opened to grasp and release tiny objects just like the flytrap leaves.

Furthermore, the DIW holds noticeable superiority in multi-material integrated printing, which is particularly intriguing for the hybrid design of actuators toward predictable motions.[130,134–136] For example, Lewis et al. localized the deformation to active CLCP hinges while utilized the stiff passive planar facets for transmission and supporting with a hybrid design of origami structure, which allowed to model and predict the motions of actuators with existing mechanical tools (**Figure 13a**).[130] The CLCP hinges with low T_{NI} (blue region) bent into valley folds upon T_{low} for reconfiguration, while the CLCP hinges with high T_{NI} (orange region) bent into mountain folds upon T_{high} for propulsion. The printed flat structure precisely reconfigured into the targeted pentagonal prism when initially heated beyond T_{low}. Subsequently, the active hinges (orange region) were heated beyond T_{high} and drove the rotation of their connected rigid facets (grey region) according to the predesigned angle, which propelled the prism to continuously roll through the interaction force between the facets and the hot stage. This work highlighted the advantages of DIW in achieving predictable and designable motions of CLCPs, thus attracting wide research interests among engineers for the considerations in soft robots.

Currently, the attainable geometries of DIW are still restrained due to the layer-wise deposition, which poses huge challenges to construct geometries with z-axis discontinuous structural characteristics. Regarding this issue, Qi et al. proposed a strategy that replaced the widely-used flat print platform with customized soluble supporting pillars, where the extruded filaments were deposited on the DLP-printed pillars with varied height to construct a hollow pyramid (Figure 13b).[137] A freestanding CLCP pyramid was obtained after the removal of soluble pillars, which exhibited reversible collapsing consistent with the results of FEA simulation. Another reported strategy is to introduce an off-center continuous aramid fiber during printing (Figure 13c).[138] The hollow structures were directly printed without assisted platforms for deposition, due to the great supporting ability of the aramid fiber for the extruded filaments. Moreover, the high modulus of aramid fibers also endowed the printed LCP actuators with outstanding bearing capacity. A freestanding pyramid and a cubic truss were printed by this strategy, where each CLCP filament bent upon heating attributed to the different coefficients of thermal expansion between aramid fiber and CLCP matrix.

The DIW regulates both the mesogen alignment and geometry with digital control, which provides significant convenience to design actuation modes through interdisciplinary approaches. On the other hand, two challenges of DIW should be overcome to further expand its application: 1) additionally achieve precise control over Z-axis mesogen alignment rather than merely that within the X-Y plane. 2) directly construct targeted exquisite structures in 3D space. This requires not only advancements in 3D printing equipment but also innovations in the processability of mesogenic inks.

3.4. Mechanical Alignment

The pursuit of enhanced geometric designability has also revived the enthusiasm for mechanical alignment, since it provides

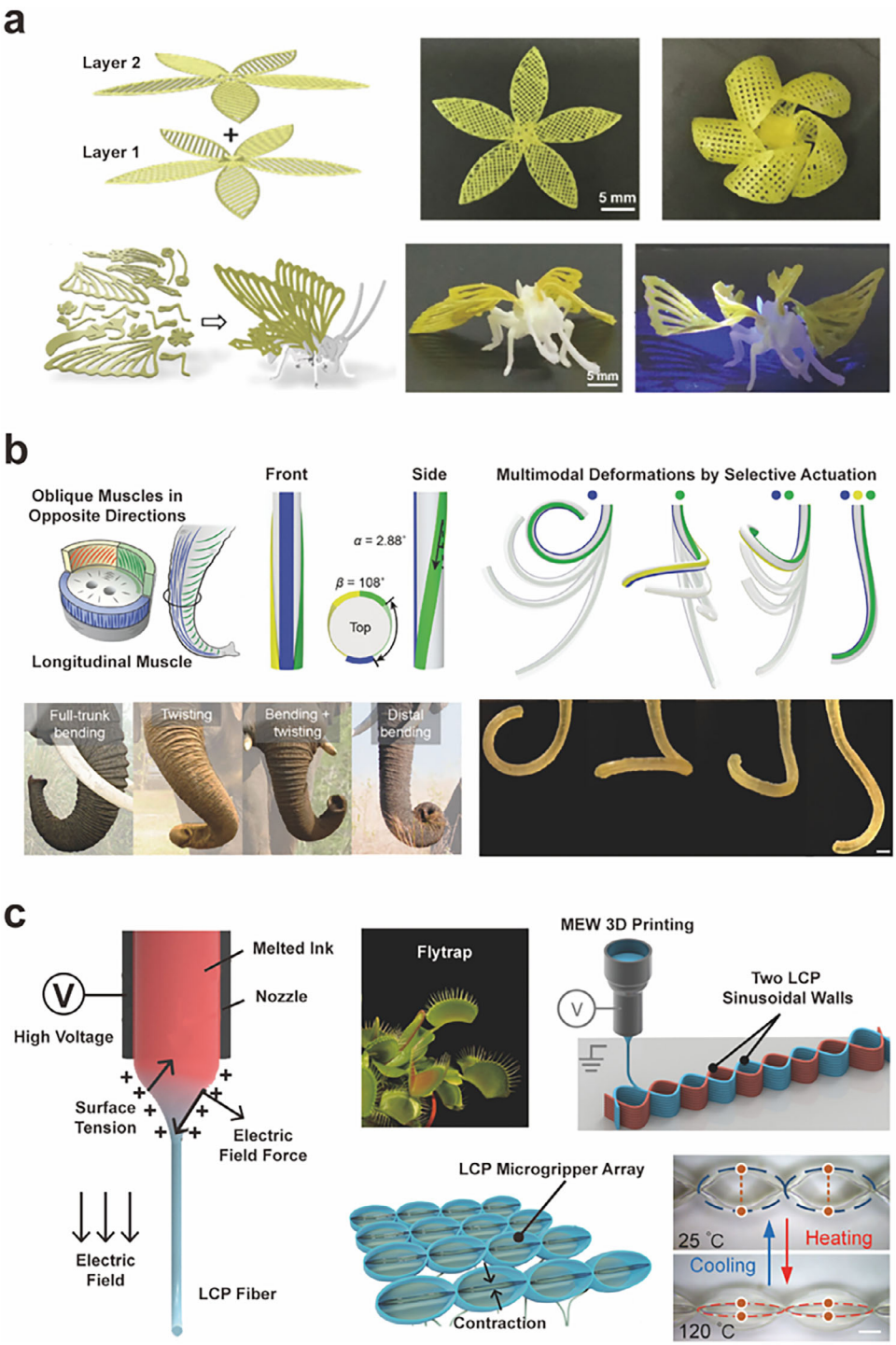

Figure 12. Nature-inspired LCP actuators printed by DIW. a) A flower-shaped LCP actuator and a hybrid butterfly-like actuator with polycaprolactone (PCL) body and CLCP wings. Reproduced with permission under the CC BY 4.0 license.[131] Copyright 2024, The Authors, published by ACS. b) An artificial elephant trunk consisted of a passive silicone rod (gray), a straight CLCP fiber (blue), and two helical CLCP fibers (yellow and green) with reverse handedness. The full-trunk bending, twisting, bending + twisting, and distal bending are achieved by driving the blue fiber only, the green fiber only, the blue and green fibers together, and all the fibers respectively. The simulation and experimental results of the multimodal deformations are demonstrated. Reproduced with permission.[132] Copyright 2024, Wiley-VCH. c) DIW printer that enables refined structures of actuators through the incorporation of an electric field for slenderer filaments. The actuation of the printed array of microgrippers is demonstrated. Reproduced with permission under the CC BY 4.0 license.[133] Copyright 2024, The Authors, published by AAAS.

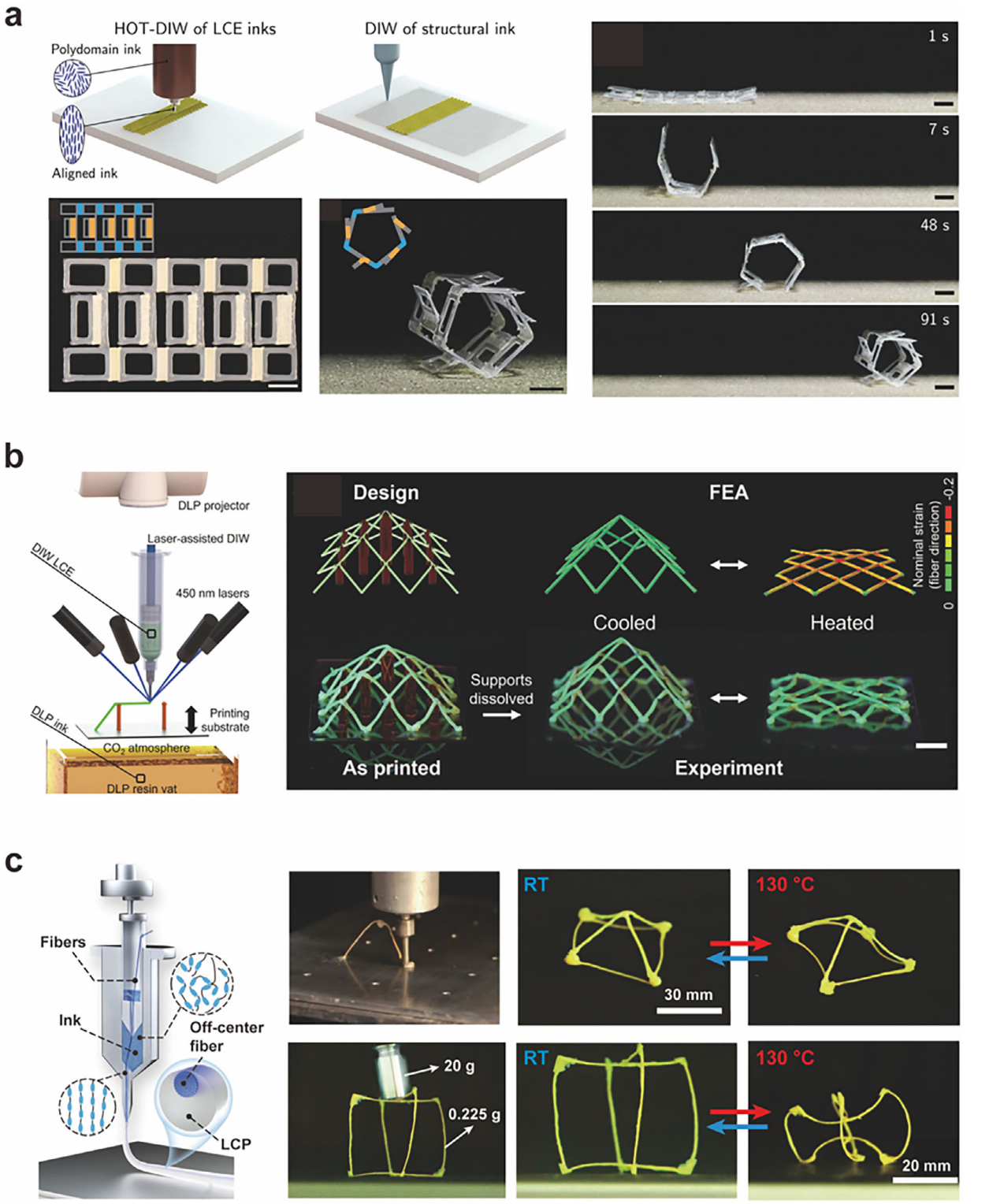

Figure 13. LCP actuators fabricated by multi-material integrated printing. a) A hybrid robot composed of active CLCP hinges and passive structural facets. The robot reconfigures at first and then rolls continuously when placed on a hot stage. Reproduced with permission.[130] Copyright 2019, AAAS. b) Schematic of a DIW-DLP hybrid 3D printer. The simulation and experimental results of the printed pyramid-shaped LCP actuator are demonstrated. Reproduced with permission.[137] Copyright 2022, Wiley-VCH. c) Schematic of a specially designed DIW setup that integrates a continuous off-center aramid fiber during printing, with the images showing the actuation and bearing capacity of the printed pyramid and cubic truss. Reproduced with permission under the CC BY 4.0 license.[138] Copyright 2023, The Authors, published by Springer Nature.

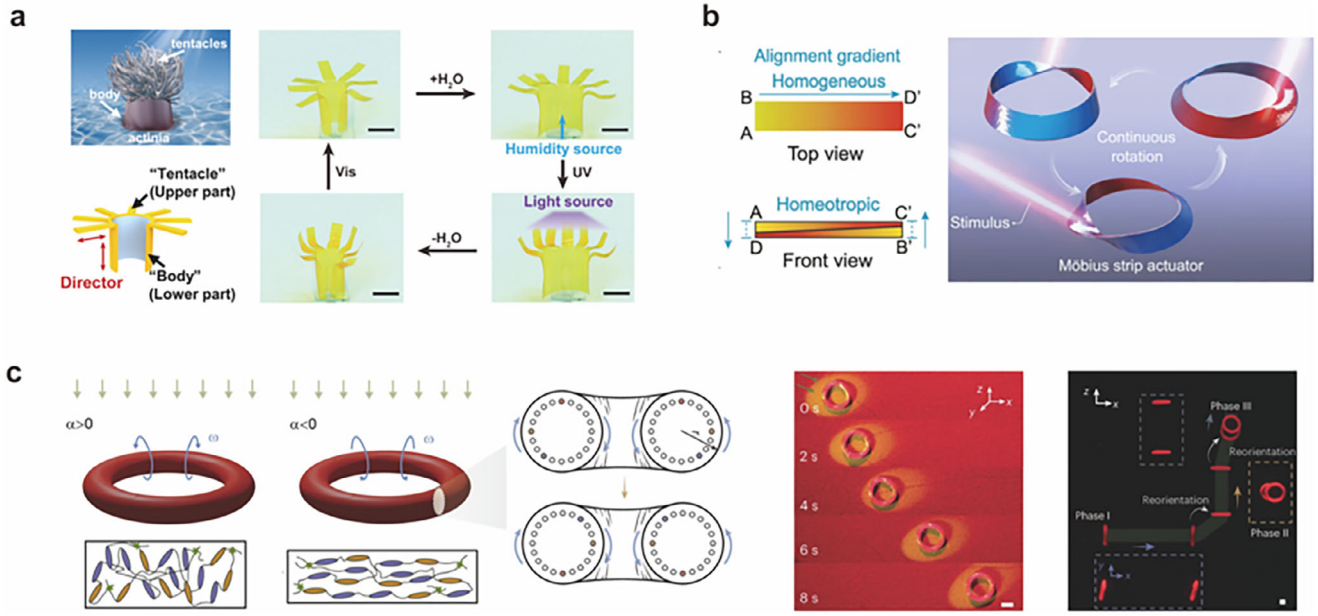

Figure 14. LCP actuators aligned by uniaxial mechanical stretching. a) An actinian-like actuator. Reproduced with permission.[30] Copyright 2023, Wiley-VCH. b) The top view and front view of a bilayer CLCP ribbon, with the extent of alignment indicated by the shade of color. The ribbon is processed into a Möbius strip that exhibits in situ continuous rotation upon light irradiation. Reproduced with permission under the CC BY 4.0 license.[150] Copyright 2021, The Authors, published by Springer Nature. c) The CLCP torus with homeotropic alignment undergoes eversion, whereas the homogeneously aligned torus exhibits inversion upon light irradiation. The steerable locomotion of the torus on a dry surface and in the Stokes regime is demonstrated. Reproduced with permission under the CC BY 4.0 license.[151] Copyright 2024, The Authors, published by Springer Nature.

a broadly available and easy-to-operate way to fabricate aligned CLCPs with large dimensions and diverse macroscopic structures from 1D to 3D. Especially, actuators with z-axis discontinuous structural characteristics that are hardly available for DIW have been achieved with the mechanically-aligned CLCPs, via simple post-programming or application of a non-uniform force field during alignment.

Generally, the mechanical alignment requires lightly-crosslinked or dynamically-crosslinked mesogenic precursors to ensure the stretchability upon external force. The preparation of lightly-crosslinked precursors was initially achieved by hydrosilylation,[23–25] and then extended to chain extension chemistry.[139] The dynamically-crosslinked precursors include the precursors with dynamic covalent networks and physical crosslinked networks, which are aligned by external force when the dynamic bonds are broken, and fully-crosslinked again through the re-formation of the dynamic bonds.[140–143]

Aligned CLCP 1D fibers and 2D films from millimeter to centimeter scale are easily available for mechanical alignment, which allows to be conveniently post-programmed into more complicated geometries by hand.[144–149] Yu et al. prepared a monodomain physically-crosslinked LCP film that was dual-responsive to light and moisture via hot stretching, and then processed the film into an actinian shape through folding and cutting.[30] Similar to actual actinia, the upper "tentacles" of the actuator bent upon the exposure of light, and the lower "body" unfolded in response to humidity (**Figure 14a**). Yang et al. made a bi-layer CLCP ribbon and processed it into an authentic Möbius [±1] strip with a one-sided, defect-free surface through twisting and adhesive bonding (Figure 14b).[150] The gradient alignment in each layer with uneven thickness was achieved under uniaxial stretching, since higher stress was induced in the thinner areas and resulted in a higher extent of alignment. The photothermal-induced gradient contraction broke the rotational symmetry of the strip with light irradiation on the locus of the twisted region, which contributed to the zero-elastic energy mode (ZEEM) for continuous anticlockwise/clockwise in situ rotation. Also, on the basis of ZEEM, Zeng et al. reported a light-steerable CLCP torus recently, which demonstrated non-trivial self-sustained rotation with tunable velocity and direction (Figure 14c).[151] A uniaxially aligned CLCP fiber was processed into a torus by looping the thick fiber and gluing its head and tail. Photothermal-induced gradient contraction was induced due to the thermal gradient across the thickness upon local light irradiation, which drove the rotation of the torus, attributed to the break of rotational symmetry. The direction of rotation was defined by the alignment-dependent thermal expansion coefficient (α), while the velocity was tunable by the light intensity and the radius of the fiber. Furthermore, optically controllable locomotion in various realms, including terrestrial, confined, fluidic environments, and even the Stokes regime, was achieved through the asymmetric friction or drag forces between the rotational torus and its surroundings.

Compared with uniaxial stretching, non-uniaxial force fields simultaneously aligns mesogens and induces asymmetric strain of the mesogenic precursors that facilitates the construction of 3D geometries (**Figure 15a–c**). The bending/folding, as the most prevalent operation to induce non-uniaxial force field in 2D films made of mesogenic precursors, enables origami-structured LCP actuators with ordered alignment built in the creases (Figure 14a).[152–156] As for the compressing, it is commonly

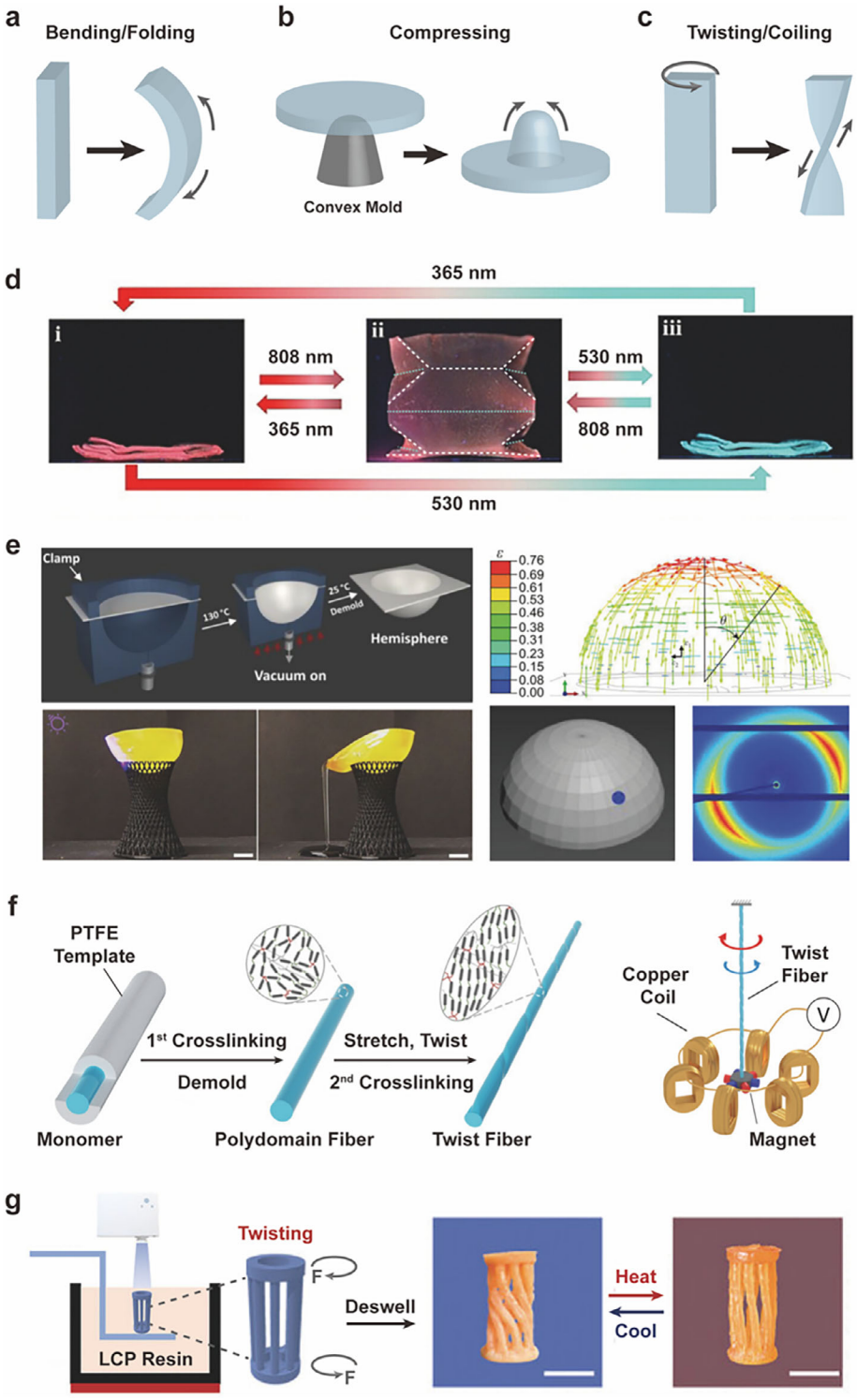

Figure 15. LCP actuators aligned by non-uniaxial force fields. Schematic illustration of the a) bending/folding, b) compressing process, and c) twisting/coiling process to simultaneously align the mesogens and program the geometry of LCP actuators. The arrow represents the direction of the induced local stress for alignment. d) An origami actuator prepared, aligned, and shaped by folding. Reproduced with permission.[152] Copyright 2021, Wiley-VCH. e) A hemisphere-shaped actuator aligned and shaped by compressing. Reproduced with permission under the CC BY 4.0 license.[164] Copyright 2024, The Authors, published by Wiley-VCH. f) A spiral fiber-shaped actuator aligned and shaped by twisting, with the illustration of an electrical generator driven by the reversible torsion of the fiber. Reproduced with permission.[161] Copyright 2022, Wiley-VCH. g) Schematic of a column-ring-shaped polydomain solid precursor printed by the DLP-based 3D printer. The solid precursor is aligned by the subsequently applied twisting process, and the obtained actuator undergoes un-twisting upon heating. Reproduced with permission.[169] Copyright 2021, Wiley-VCH.

used to fabricate convex actuators by embossing the films with a punch-pin, where the ordered alignment is distributed on the walls of the bulge (Figure 15b).[157] The coiling/twisting is commonly applied to 1D fibers, which induces a spiral geometry and rotating alignment along the longitudinal axis (Figure 15c).[158–163] The solid mesogenic precursors treated by non-uniaxial force field mentioned above achieve 3D structures and region-specific alignment at the same time, which are fixed by the second crosslinking or re-crosslinking. Accordingly, LCP actuators with intriguing geometries and actuation modes have been directly obtained without the post-programming of CLCPs.

Li et al. prepared a photoresponsive origami structure by folding the film-shaped solid precursor, with the creases served as active hinges.[152] The obtained CLCP film preformed discoloration-accompanied bending-unbending along the creases upon the exposure to light at different wavelengths (Figure 15d). Schenning et al. attempted the vacuum thermoforming instead of the commonly-used embossing to fabricate convex LCP actuators, which was a mature method used in the industrial manufacturing of commercial polymers.[164] When the heated, film-shaped solid precursor was sucked into the hemisphere mold under vacuum, an angular-dependent alignment was formed on the hemispherical wall by region-specific stresses (Figure 15e). The photodeformable hemisphere was filled with water initially, which released the water from the spout upon local UV light irradiation along the lip. Yang et al. established rotating alignment and achieved significant thermal-induced torque of the CLCP fiber through twisting the fiber-shaped solid precursor.[161] The twisted fiber served as the driving unit in an electrical generator system, rotating six magnets and harvesting electrical energy upon alternative heating and cooling (Figure 15f).

The shapes of solid precursors were further extended to preformed 3D structures by molding or direct printing.[165–168] For example, Yang et al. printed a column-ring-shaped polydomain solid precursor by DLP and aligned it through twisting, which displayed a reversible un-twisting with a large actuation strain upon heating (Figure 15g).[169] Precursors with various interesting 3D structures, such as the hollow lattice, the Eiffel Tower, and the mermaid have been attempted.[167,168] Through the proper choice of the subsequently applied external force, ordered alignment for anisotropic deformation was built while most of their original structural characteristics were maintained.

The mechanical alignment is particularly attractive for researchers beyond LCP chemists due to the easy-to-operate and broadly accessible characteristics. So far, the principal researches of LCP actuators aligned by mechanical force have focused on the macroscale structural design, with little attentions paid to the precise patterning and diversification of mesogen alignment. The synergistic regulation of the mesogen alignment and geometries still desires deeper exploration, to unlock the full potential of mechanical alignment.

3.5. Self-Assembly for Mesogen Alignment

The annealing-induced self-assembly was used to align the mesogens for photodeformable LCP actuators by Yu et al. in 2016.[170] We developed a kind of high-molecular-weight linear LCP (LLCP) via the ring-opening metathesis polymerization (ROMP), where the flexible rubber-like alkyl backbone and long spacers provided the azobenzene mesogens enough free volume to self-assemble into a smectic C phase (**Figure 16**a). The chemical heterogeneity between the flexible alkyl backbone and the rigid aromatic mesogens promoted microphase separation, resulting in nanoscaled lamellar structure that consists of segregated main-chain and side-chain sublayers. These sublayers act as a dual physical crosslinked network of LLCP, ensuring the reversibility of photodeformation. Moreover, the annealing-induced alignment was observed to vary from in-plane (smectic A phase) to out-of-plane (smectic C phase) as the spacer length increased, which governed the bending direction and amplitude of LLCP films upon light (Figure 16b).[171]

The annealing-induced self-assembly also occurred in copolymerized LLCPs. Other mesogens, such as biphenyl or phenyl benzoate mesogens, were incorporated into the LLCPs by direct copolymerization and coassembled with azobenzene mesogens into the ordered LC phase upon annealing (Figure 16c,d). The incorporation of biphenyl mesogens effectively increased the light penetration depth compared with the homopolymerized azobenzene-containing LLCP films, contributing to enhanced photodeformability (Figure 16c).[172] The introduction of phenyl benzoate mesogens promoted the self-assembly via the activation of chain mobility. Accordingly, a highly ordered smectic B phase was further observed in this copolymerized LLCP treated with post-tension annealing (Figure 16d).[173] The tension-induced strain energy was locked by the smectic B phase, and subsequently released by photochemical phase transition that disrupted the ordered alignment. An ultralarge light-driven contraction rate up to 81% was achieved by the annealed post-tension LLCP fiber through the release of stored strain energy.

Remarkable chain entanglement, formed in LLCPs due to their high molecular weight, contributes to robust mechanical properties, including a moderate elastic modulus (96 ± 19 MPa), high toughness (319 ± 41 MJ m^{-3}), high strength (≈20 MPa) and a large fracture strain ($2089\% \pm 275\%$) (Figure 16e). Furthermore, the thermodynamic and mechanical properties of LLCPs exhibit a broad tunable range, owing to the excellent designability of their molecular and phase structures (Figure 16f).

The LLCPs also exhibit great compatibility with existing industrial processing methods due to the absence of a chemical crosslinked network. Various geometries from 1D to 3D, including fibers, films, and microtubes, have been conveniently shaped with LLCPs through commonly used melting and solution processing methods (**Figure 17**a), which performed reversible deformation by a subsequently applied annealing treatment.[170–175] The decouple of shaping and alignment largely enriches the available geometries and dimensions of LCP actuators, which broaden the potential applications of LCP actuators in diverse usage scenarios.

The fiber-shaped LLCPs were prepared into interesting actuators through textile or twisting processing. A string bag was constructed via the combination of passive sewing threads and the annealed post-tension LLCP fibers, whose ultralarge light-driven contraction closed the bag that held two plastic balls (Figure 17b).[173] Another kind of multifunctional LLCP was twisted into a spring-like structure. Upon heating, the spring exhibited a self-propelled rolling along with the fluorescence dimming (Figure 17c).[176] The film-shaped LLCPs featuring linear

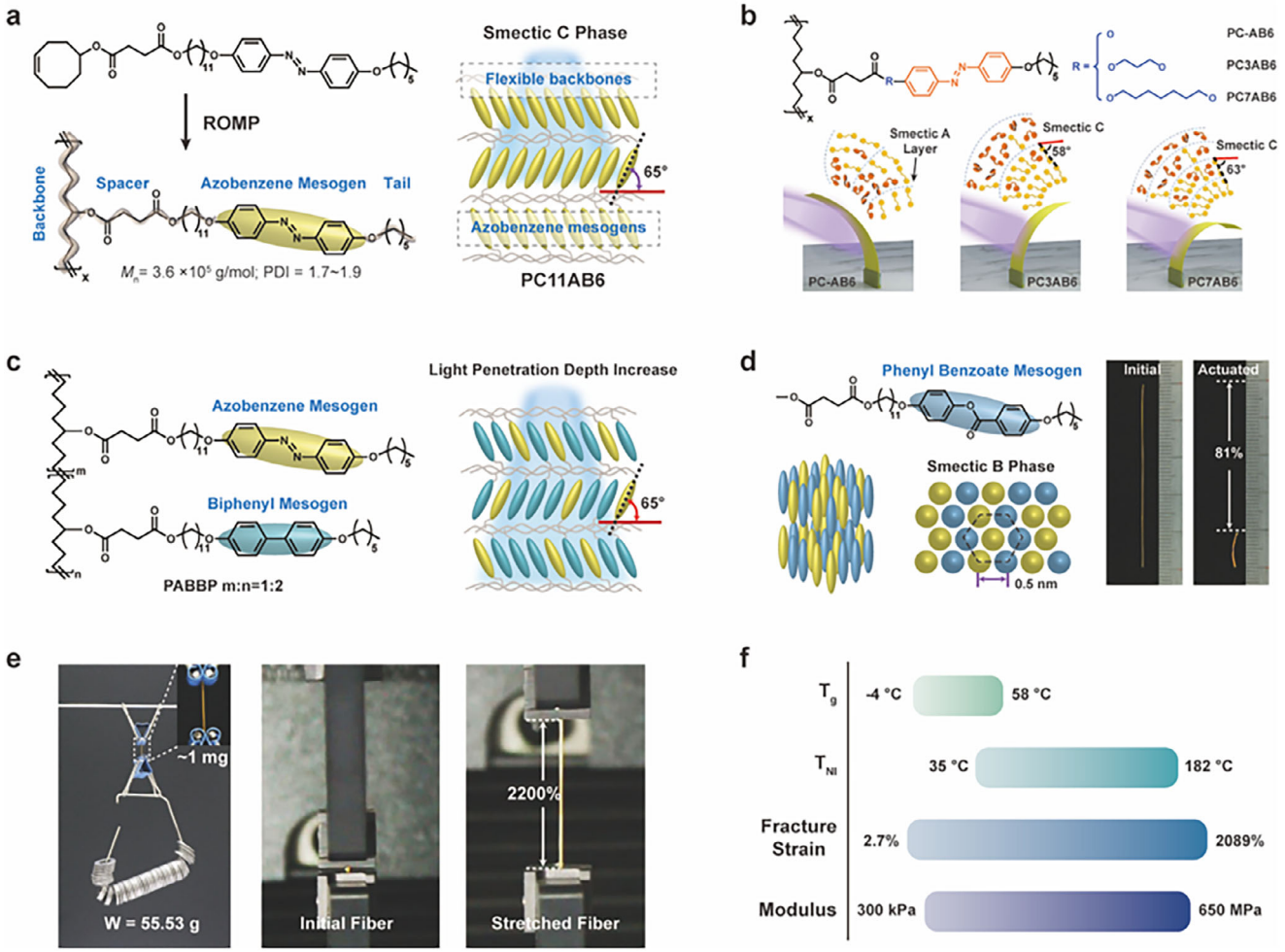

Figure 16. Chemistries of smectic linear LCPs (LLCPs) and their available phase structures via self-assembly. a) Molecular structure of an azobenzene-containing linear LCP (LLCP) and the schematic illustration of the smectic C phase built in the LLCP via annealing-induced self-assembly. Reproduced with permission.[170] Copyright 2016, Springer Nature. b) Molecular structures of LLCPs with varied spacers, and the corresponding changes in phase structure and bending behavior. Reproduced with permission under the CC BY 4.0 license.[171] Copyright 2019, The Authors, published by Wiley-VCH. c) A copolymerized LLCP that spontaneously self-assembles into the smectic C phase via annealing, with the schematic showing the increased light penetration depth within the lamellar structure. Reproduced with permission.[172] Copyright 2019, Wiley-VCH. d) Molecular structure of the phenyl benzoate side-chain within a copolymerized LLCP, with the schematic showing the highly ordered smectic B phase obtained via post-tension annealing. The images show the ultralarge light-driven contraction up to 81% of the LLCP fiber. Reproduced with permission.[173] Copyright 2020, Wiley-VCH. e) Images showing the mechanical strength and toughness of LLCP fibers, including a fiber sample supporting iron rings strung by an iron wire, and another sample stretched to 22 × its initial length. f) The tunable range of thermodynamic and mechanical properties of LLCPs.

structures enable seamless integration with other polymer materials, thus facilitating the design of multilayer thin-film devices. A multilayer, neuron-readable artificial photoreceptor was constructed without additional adhesives (Figure 17d).[175] Within this device, photo-induced stress generated in the LLCP layer is transferred to the piezoelectric P(VDF-TrFE) layer, inducing electrical signals through changes in dipole density. The large photodeformation of LLCPs promoted the efficiency of light-stress-electricity conversion, contributing to a 19-fold enhancement in open-circuit voltage (0.79 ± 0.02 V) compared to previous works. Visual image recognition was further achieved via a 25-unit pixelated photoreceptor. We also designed a bionic "flower and butterfly" with LLCP films.[156] The kirigami-structured photodeformable LLCP film acted as the butterfly, while the LLCP films exhibiting light-induced shape memory effect were welded into a floral shape (Figure 17e). The "flower" bloomed upon UV light, and the "butterfly" flapped its wings upon alternative irradiation of UV and visible light.

In particular, the LLCPs hold noticeable superiority in the fabrication of microscale 3D actuators. Their great compatibility with a series of melting/solution processing methods facilitate the construction of geometries with exquisite 3D microstructures. Moreover, the annealing-induced self-assembly strategy ensures to align mesogens in a non-contact way that avoid the distortion of the desired geometry. We utilized the azobenzene-containing LLCPs to fabricate photodeformable tubular microactuators (TMAs) and achieved all-optical microfluidic transportation for the first time (Figure 17f).[170] The LLCP was initially

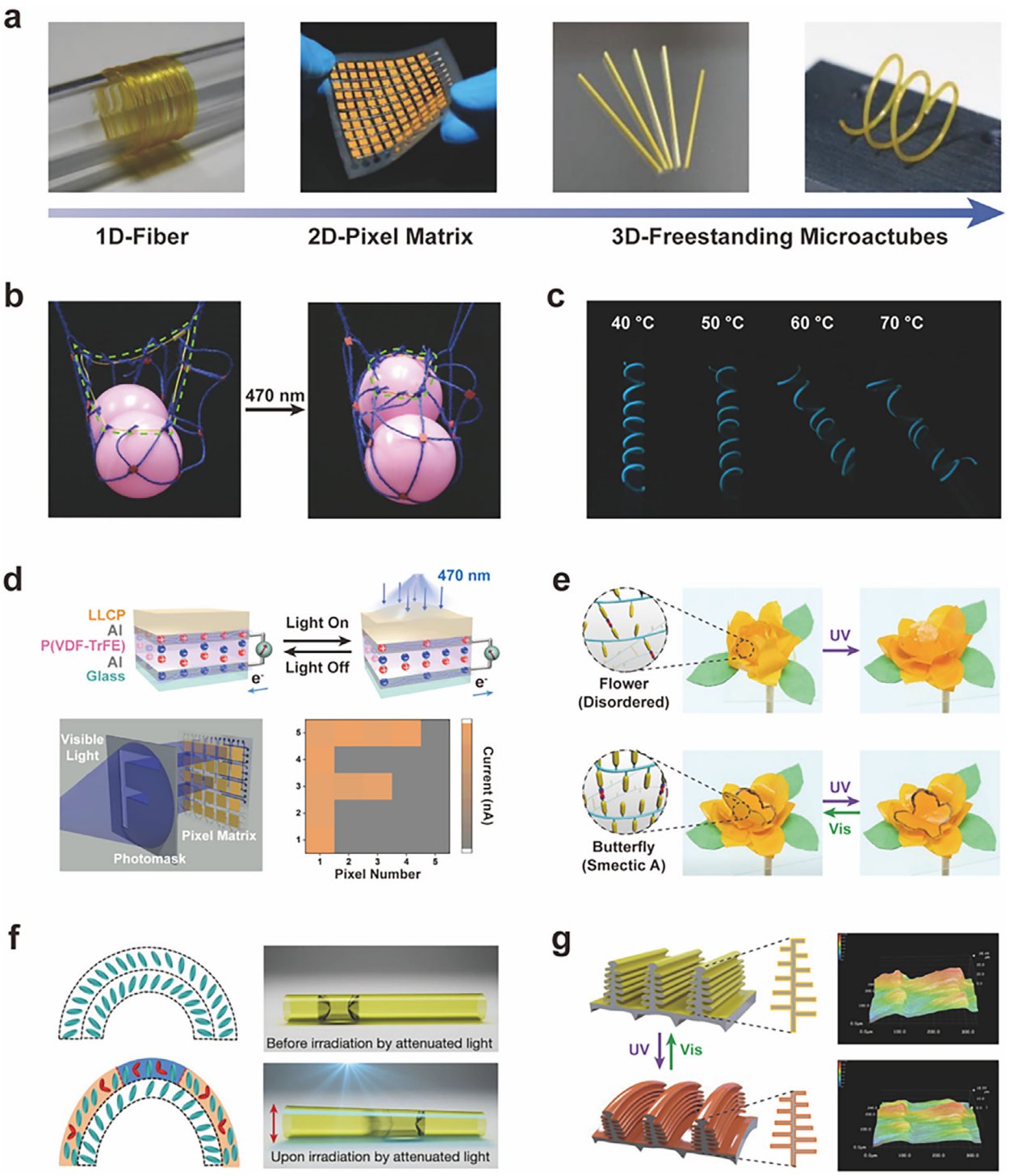

Figure 17. LCP actuators aligned via self-assembly. a) LLCP actuators from 1D to 3D. Reproduced with permission.[170,175] Copyright 2020, Wiley-VCH; Copyright 2016, Springer Nature. b) A string bag composed of LLCP fiber and passive sewing threads, with the dashed green lines outlining the LLCP fiber. Reproduced with permission.[173] Copyright 2020, Wiley-VCH. c) A spring-shaped LCP actuator. Reproduced with permission.[176] Copyright 2025, Wiley-VCH. d) Schematics showing the conversion of light-stress-electric signals within the artificial photoreceptor, and the visual image recognition achieved by pixelated photoreceptor. Under mask-patterned illumination, each irradiated pixel generated a measurable photocurrent, enabling reconstruction of the optical pattern "F". Reproduced with permission.[175] Copyright 2023, Wiley-VCH. e) A bionic "flower and butterfly" prepared by LLCP films. Reproduced with permission.[156] Copyright 2022, Wiley-VCH. f) The axial asymmetric deformation of a tubular LLCP microactuator upon attenuated irradiation, with the cross-sectional schematic showing the alignment change before and upon irradiation. Reproduced with permission.[170] Copyright 2016, Springer Nature. g) Schematics and 3D reconstruction images showing the hierarchical deformation of the microstructures of the Morpho butterfly wing driven by photodeformable LLCP coating. Reproduced with permission.[174] Copyright 2018, Wiley-VCH.

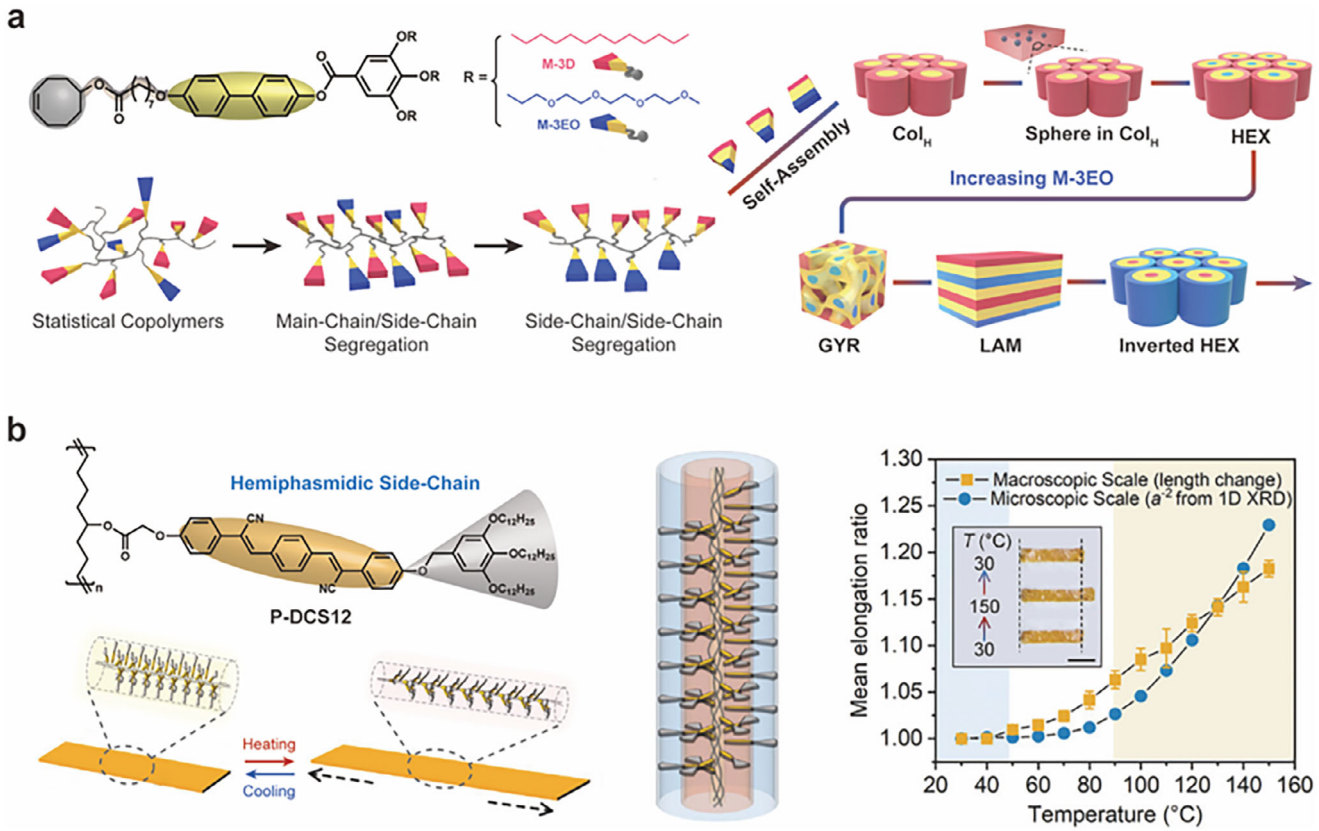

Figure 18. Chemistries of hemiphasmidic LLCPs and their available phase structures via self-assembly. a) Chemical structures of hemiphasmidic monomers with different peripheral tails of wedges. As the molar fraction of M-3EO in copolymerized LLCPs increased, the resulted phase structures experienced diverse variations. Reproduced with permission.[177] Copyright 2024, ACS. b) Molecular structure of the hemiphasmidic LLCP containing rod-like dicyanodistyrylstilbenzene mesogens and bulky fan-like tail groups, which self-assembles into a columnar phase featuring the "core-shell-corona" structure via post-compression annealing. The core is composed of polymer chains, the shell is the mesogens, and the corona is the fan-like tail groups. This LLCP film featuring columnar units shows negative thermal expansion upon heating, with its linear elongation behavior demonstrated in the right panel. Reproduced with permission.[178] Copyright 2023, Wiley-VCH.

coated in a glass capillary by solution evaporation, and the capillary was etched after the annealing treatment. The obtained TMA performed asymmetric shape change from cylindrical to conical upon the irradiation of attenuated 470 nm light, which induced capillary forces to propel the inner fluid slug toward the narrower end. We even designed a photodeformable 3D micro/nanostructure by combining LLCPs and the Morpho butterfly wing (MBW) template (Figure 17g).[174] The azobenzene-containing LLCPs was made into microfibers through electrospinning and then well-distributed on MBW via fused deposition. Ordered alignment was built in the resulted LLCP coating by annealing, which drove the hierarchical deformation of MBW upon light irradiation. The combined fused deposition and self-assembly strategies maximized the preservation of 3D micro/nanostructural integrity by preventing damage from solvent exposure and mechanical forces to the delicate hierarchical architecture of MBW. The hierarchical deformation, including the structural changes of scales, ridges, and lamella spacing, induced the blueshift of the reflection peak (69 nm) and the variation of reflection intensity (40%).

Beyond our efforts, Chen et al. have also explored the phase structure and actuation characteristics of LLCPs.[177–179] They synthesized a series of copolymerized LLCPs with two kinds of hemiphasmidic cyclooctene monomers, whose tail groups differed in the peripheral tails of the wedges (**Figure 18a**).[177] Microphase segregations between main chains and side chains first occurred in the obtained statistical copolymers, and the separation of side chains was further observed due to the genuine immiscibility between M-3D and M-3EO. This phenomenon led to a kind of new structural motifs, where the main chain adopted a tortuous conformation and sandwiched between domains formed by M-3D and M-3EO respectively. The aspects and curvatures of these motifs varied as the molar fraction of M-3EO increased, which promoted the formation of diverse unique phase structures, including hexagonal columnar (Col$_H$), hexagonally packed cylinder (HEX), double gyroid (GYR), lamella (LAM) and inverted HEX. These unique phase structures may endow the deformation of LLCPs with some non-trivial properties. For example, most reported LCP actuators exhibited deformation in a two-state way rather than continuous multi-state manner, since their stimuli-responsive deformation were realized via the sharp phase transition from ordered to disordered. This constraint was ingeniously circumvented in the LLCP with columnar phase, which utilized the continuous negative thermal expansion of the

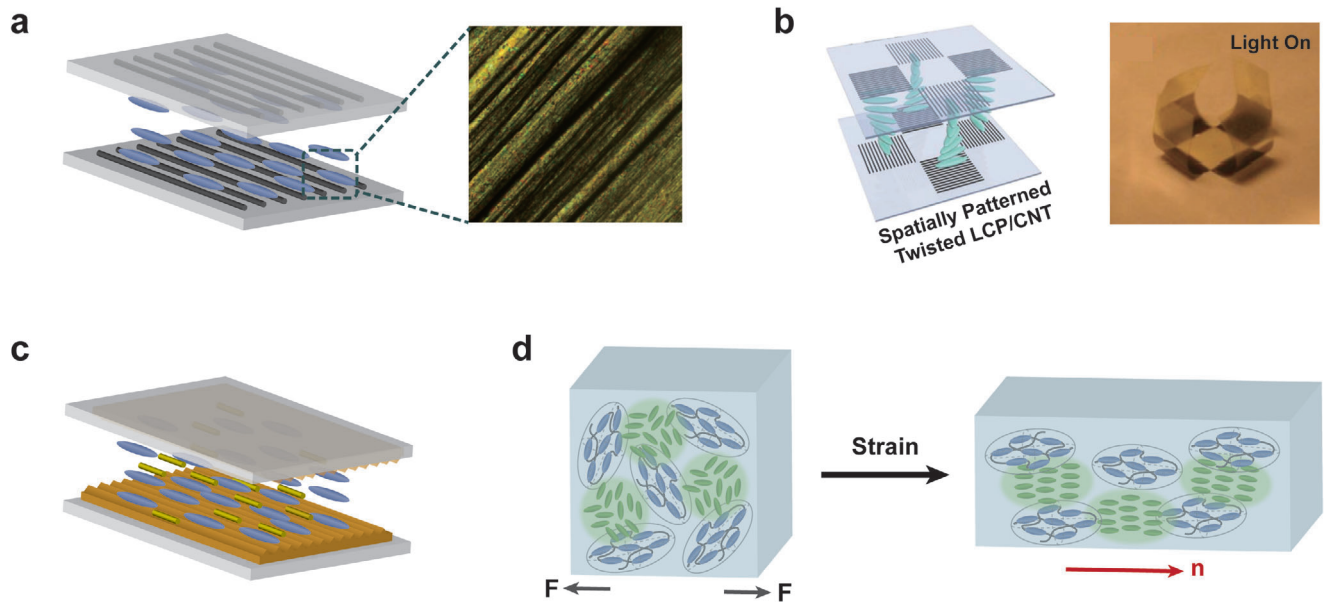

Figure 19. The cooperative alignment of mesogens and anisotropic nanofillers. a) The coating composed of highly-oriented anisotropic nanomaterials serves as the alignment layer to anchor the mesogens. The black rods represent the uniaxially aligned nanofillers. Reproduced with permission.[183] Copyright 2012, Wiley-VCH. b) An CLCP origami actuator with twisted mesogen alignment built in the creases. Reproduced with permission.[184] Copyright 2019, Wiley-VCH. c) The aligned mesogens arrange the anisotropic nanomaterials (yellow rods) along the director of the mesogens. d) The incorporated unreactive LCs (green rods) form phase-separated domains. Upon stretching, the mesogens and incorporated LCs cooperatively align.

columnar assemblies below T_{NI} to induce macroscopic deformation (Figure 18b).[178] The microscale columns elongated linearly due to the rejections of the surplus molecules with the increase of temperature, thus ensuring the precise control of the macroscopic continuous expansile-contractive deformation, just like the actual biological muscles.

The LLCPs simultaneously possess moderate elastic modulus, high toughness, high strength and large elongation at break due to the high molecular weight and ordered lamellar structure. Combined with the excellent designability of molecular structures, tunability of LC phase and processing properties, the LLCPs show great potentials in creating high-performance actuators capable of even more complicated bionic motions. However, the high-threshold synthesis of these LLCPs results in obstacles to their popularization currently.

4. Nano-Composition Used in LCP Actuators

Apart from the actuation modes, the actuation performances of the LCP actuators also have a non-negligible influence on the practical achievable actuations. For example, the rapid large deformation is essential to achieve explosive actuations, while the output force and mechanical properties directly determine the work capacity and bearing capacity of actuators.[57,180–182] Various strategies have been reported to regulate the actuation performance for broader usage scenarios, and the nano-composition is particularly appealing due to its easy operations and high efficiency.[21] Especially, the incorporation of rod-like nanomaterials additionally facilitates the mesogen alignment attributed to their anisotropic structures.[183–185] We proposed the nanomaterial-assisted alignment approach for the first time. Uniaxially aligned CNTs were coated on an LC cell, which oriented the mesogens along the CNT alignment axis via the surface anchoring effect (**Figure 19a**).[183] Furthermore, Ware et al. locally induced twisted alignment of mesogens by patterning the CNTs, thus achieving an origami actuator with photodeformable hinges (Figure 19b).[184]

The mutual interactions between anisotropic moieties also drive the self-organization of nanomaterials surrounded by aligned mesogens.[186–190] Yang et al. uniaxially aligned the mesogens via the surface-enforced alignment, which arranged the incorporated gold nanorods (AuNRs) along the director of the mesogens through the attractive intermolecular forces (Figure 19c).[191] When subjected to external mechanical force, the mesogens and anisotropic nanomaterials exhibit cooperative alignment along the loading axis (Figure 19d).[192–195] Shahsavan et al. incorporated non-reactive low molecular weight LCs in CLCPs, inducing phase-separated microdomains at micro- to nano-scales.[196] Upon stretching, the LC/CLCP composite was aligned while the LC microdomains underwent a phase transition from disordered to short-range smectic ordering.

Direct mixing of CLCPs with certain nanomaterials, including carbon black (CB), graphene, and carbon nanotubes (CNTs), effectively improves power density and stiffness of LCP actuators.[197–200] However, the incorporation of these rigid nanofillers often results in reduced extensibility and actuation strain of LCP actuators, especially at high loading levels. Recently, several non-traditional methods of nano-composition have been developed, which offer potential approaches to balance mechanical properties and large actuation strain. For example, the LC/CLCP composite designed by Shahsavan et al. achieved the enhancement of stiffness without compromising thermal-responsive strain, since the LC microdomains acted as physical crosslinking points and introduced additional smectic

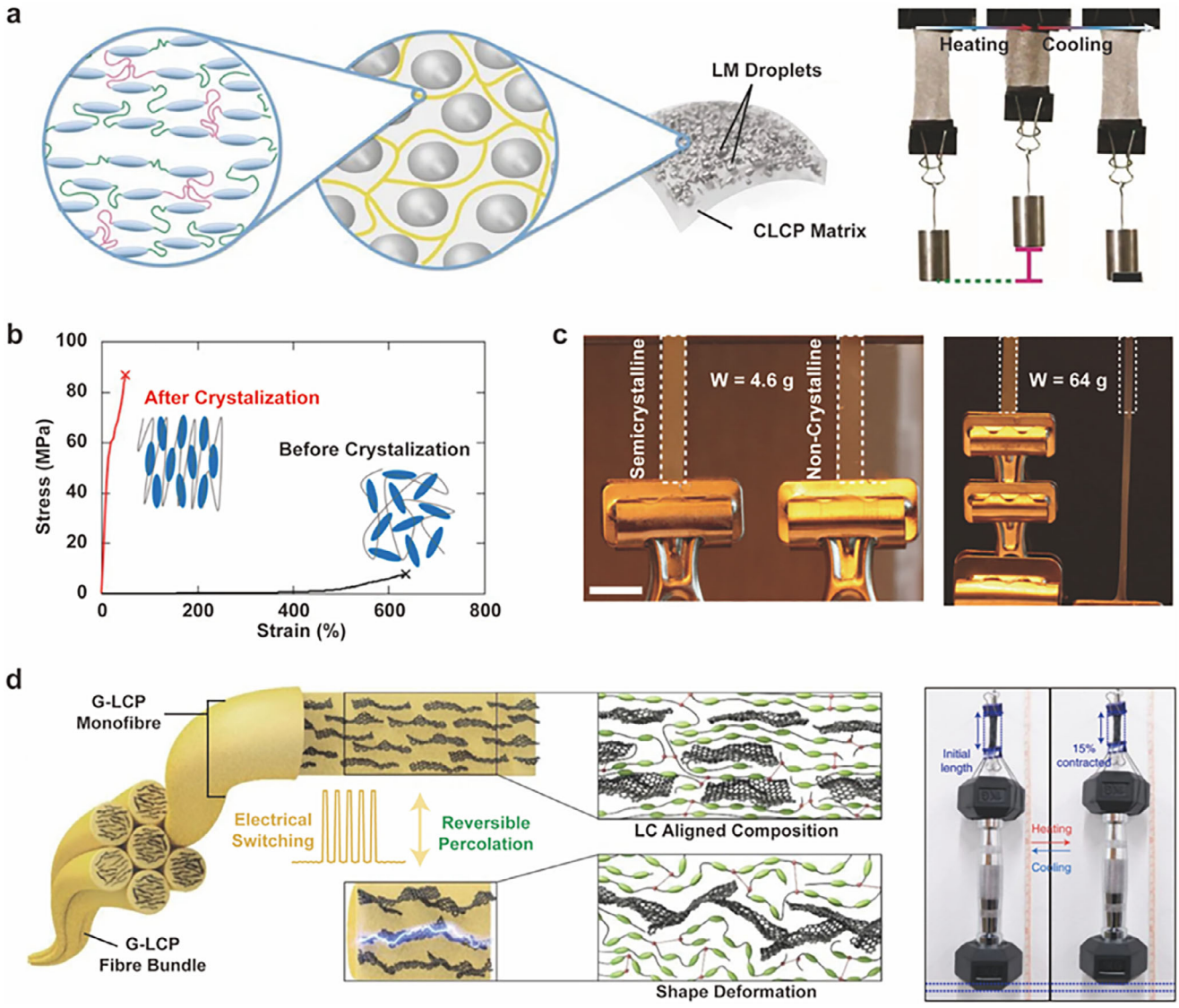

Figure 20. Mechanical enhancement achieved by nano-composition. a) The schematic shows mesogens maintain ordered alignment despite high LM droplet content in LM/CLCP film. Photographs demonstrate that the film sustains a blocking stress of ~45 kPa upon heating. Reproduced with permission.[201] Copyright 2019, National Academy of Sciences. b) The stress-strain curve of CLCPs before and after crystallization. Reproduced with permission.[203] Copyright 2017, ACS. c) The load-bearing test of semicrystalline and non-crystalline CLCP films. Reproduced with permission.[204] Copyright 2022, ACS. d) Uniaxially aligned graphene/CLCP composite fibers with thermodynamic percolated graphene network. The actuator consisted of a 1000-strand bundle of the composite fibers lifts a 1 kg dumbbell upon heating. Reproduced with permission under the CC BY 4.0 license.[205] Copyright 2022, The Authors, published by Springer Nature.

ordering.[196] Besides the LCs, the microscale liquid metal (LM) droplets are equally noteworthy. Majidi et al. first introduced LM droplets (200–500 μm in diameter) into CLCPs, establishing the concept of replacing rigid fillers with soft, deformable alternatives (**Figure 20a**).[201] They observed that the incorporation of LM droplets did not adversely affect the extensibility and actuation strain of CLCPs even at high loading levels. Yang et al. further discovered that the incorporation of LM droplets obviously enhanced the fatigue resistance of CLCPs (>2000 cycles).[202] The ultrahigh fatigue resistance might derive from two aspects: 1) the fluidic and soft LM droplets serve as stress concentration points. 2) the metal-sulfur interaction affords extra physical associations to reinforce the CLCPs. In addition to novel fillers, Ware et al. explored an in situ nanocomposite strategy based on crystallization (Figure 20b).[203] The resulting hierarchical crystalline domains enhanced the modulus by 2-fold and toughness by 5-fold, contributing to a remarkable work capacity of 730 kJ m^{-3}. Under a load of 0.5 MPa, the semicrystalline CLCP retained complete structural integrity, whereas its non-crystalline counterpart underwent significant elongation (Figure 20c).[204]

Toward practical utilizations, robust mechanical properties beyond T_{NI} are desired by LCP actuators since they decide the actual output driving force and bearing capacity. However, the mechanical properties of LCP actuators dramatically weaken across

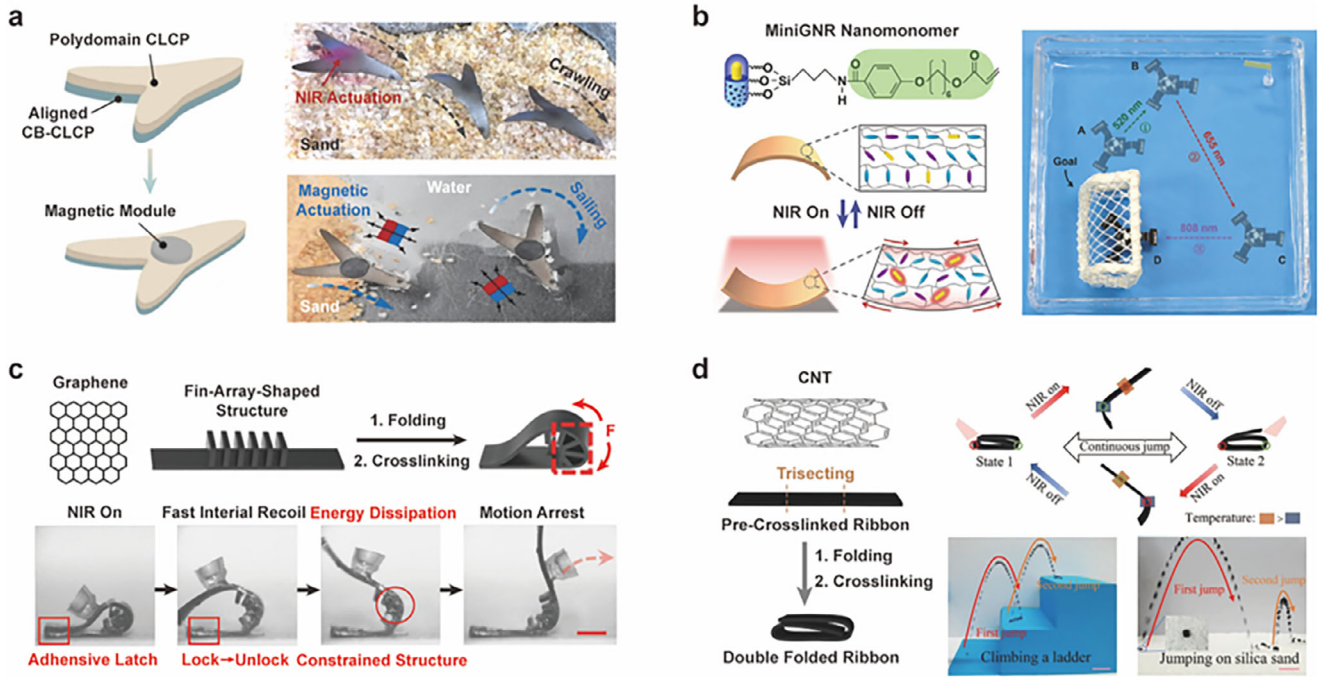

Figure 21. Light-controlled actuators made by CLCP nanocomposites. a) A cross-domain actuator obtained by assembling CB/CLCP film with a magnetic-responsive module. Reproduced with permission.[208] Copyright 2024, Wiley-VCH. b) A tri-legged water strider robot obtained by assembling the splay-aligned AuNR/CLCP composite films and the superhydrophobic copper foams. The three legs are responsive to the light at wavelengths of 520, 655, and 808 nm, respectively, since they are incorporated with AuNRs featuring distinct aspect ratios. The robot demonstrates steerable multi-directional water walking to transport cargo upon sequential irradiation of light at different wavelengths. Reproduced with permission.[210] Copyright 2022, Elsevier. c) A graphene-containing catapulting actuator with a constrained fin-array-shaped structure. Reproduced with permission.[212] Copyright 2022, Wiley-VCH. d) The left schematic shows the fabrication process a double-folded CNT/CLCP composite ribbon. The right schematic exhibits the mechanism of continuous jumping, with images showing the climbing on ladder and jumping on silica sand. Reproduced with permission.[213] Copyright 2023, Wiley-VCH.

the anisotropic-to-isotropic phase transition in most cases due to the loss of LC ordering. The helical twisting and coiling of CLCP fibers are the mainstreamed approaches for this problem, while the thermodynamic networks that strengthen with the increase of temperature appear as another intriguing solution. Kim et al. introduced the thermodynamic percolated graphene network in LCP actuator, where the graphene platelets were separated at ambient temperature and formed a continuous percolated network beyond T_{NI} (Figure 20d).[205] Attributed to the strengthened network, the Young's modulus and tensile stress of this actuator exhibited an unexpected increase at elevated temperature. The obtained nanocomposite actuator achieved excellent bearing capacity, work capacity (650 J kg^{-1}), and power density (293 W kg^{-1}), which were robust enough to lift a dumbbell 5000 times heavier than its bodyweight.

The incorporation of photothermal nanomaterials, such as MXene, CNTs, and CB, offers a simple approach to design LCP actuators with non-contact local control capability.[206,207] Chen et al. constructed a three-legged bilayer actuator composed of an aligned CB/CLCP layer and a passive polydomain CLCP layer, which crawled on the sand through localized heating upon NIR irradiation.[208] They subsequently assembled a magnetic-responsive module on the actuator, realizing its manipulation on the water surface under directional magnetic fields (**Figure** 21a). Actuators capable of explosive motions were further achieved by fully utilizing the high actuation performance of CLCP nanocomposites.[185,209] Feng et al. designed a water strider robot through the assembly of CLCP films and copper foams (Figure 21b).[210] The splay-aligned CLCP films incorporated with AuNRs were used as the legs of the robot, which propelled the robot to move unidirectionally on the water surface by rapid large bending. The superhydrophobic copper foams served as the body and feet of the robot that were responsible for the weight-bearing and drag-reducing ability, respectively. Upon selective and sequential irradiation on the legs, the robot transported a football according to the predesigned route.

The catapulting and jumping are also available for CLCP nanocomposites on the basis of specially designed bistable structures.[211] Lv et al. designed a graphene-containing LCP catapult featuring constrained fin-array structure (Figure 21c).[212] The temperature-sensitive acrylate adhesive was used to latch the accordion-like actuator, which suppressed the photothermal-induced unfolding of the right arched area to accumulate and store the strain energy. Subsequently, the left latch was unlocked upon local irradiation, which came along with the instantaneous release of substantial strain energy and an ultrafast catapulting motion like the ejection of fern sporangia. The direction of catapulting was controlled by the number and position of the constrained fins, which produced inward tension to suspend the fast opening at a well-defined angle. Similarly, Yang et al. designed a light-driven jumping robot though shaping the CNT/CLCP ribbon into a double-folded structure, where the ordered alignment

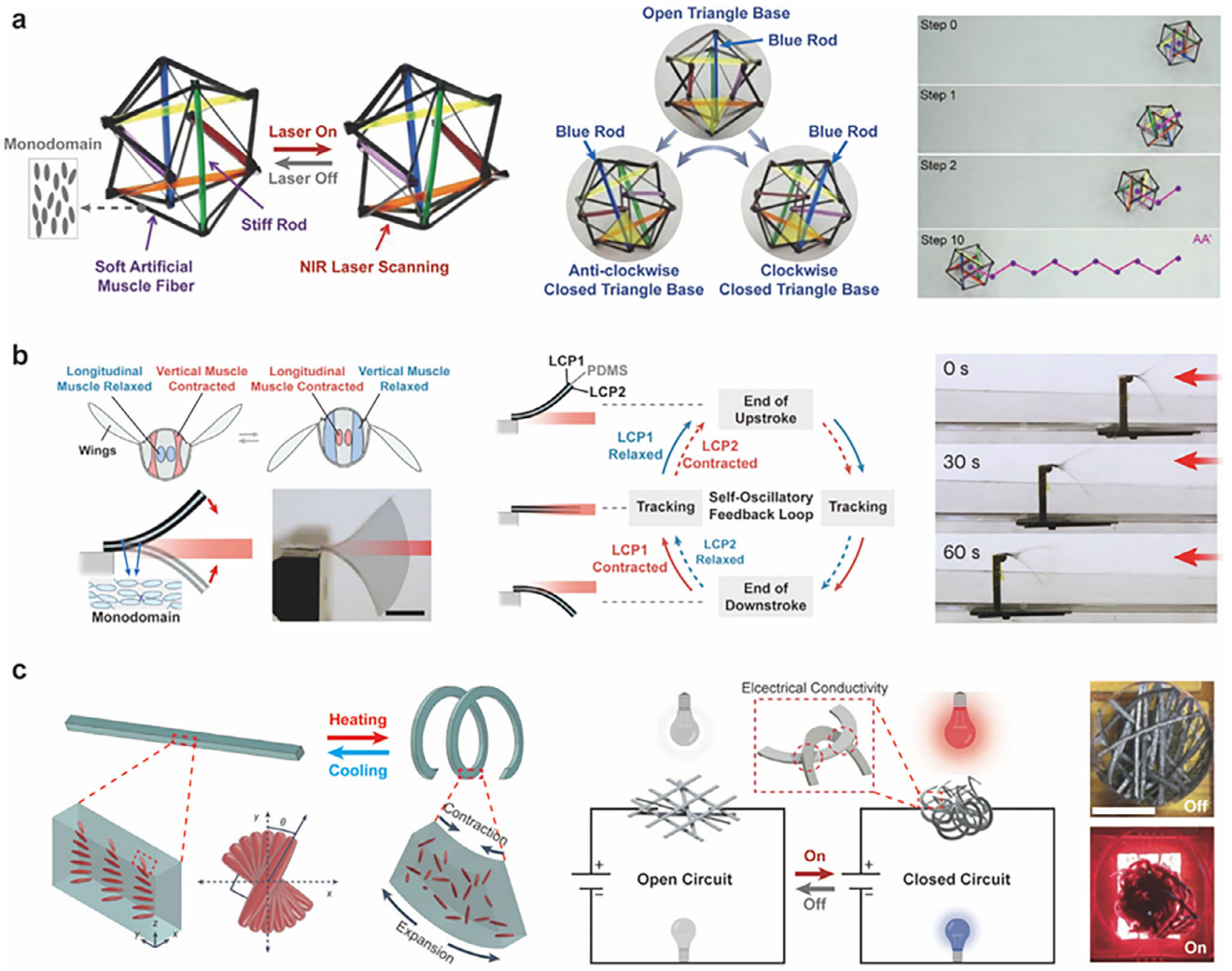

Figure 22. CLCP nanocomposite actuators capable of more complex motions through ingenious structural design. a) A tensegrity robot consisted of CNT/CLCP composite fibers and passive stiff rods, whose base of support transitions between an open triangle and a (anticlockwise or clockwise) closed triangle upon single-fiber actuation. The photographs demonstrate a zigzag rolling path of the robot powered by light. Reproduced with permission.[214] Copyright 2018, Wiley-VCH. b) A light-powered self-oscillator composed of two candle-soot-containing monodomain CLCP layers (LCP1, LCP2) and a sandwiched PDMS layer, where the CLCP layers exhibit antagonistic contraction/relaxation behavior under constant illumination. The sequential snapshots illustrate the self-oscillator propelling a sailboat on water. Reproduced with permission.[215] Copyright 2024, Springer Nature. c) Schematic showing the actuation of an individual twisted-aligned CLCP ribbon, with the offset angle θ denoting the angle between the ribbon's longitudinal axis and the orientation director on the top surface. The ribbons with LM-coating transition from an insulating to a conductive state due to the photo-induced entanglement. Reproduced with permission.[216] Copyright 2024, Springer Nature.

was built in the creases (Figure 21d).[213] The outer crease constrained the photothermal-induced unfolding of the inner crease to accumulate and store the strain energy. Subsequently, the energy was instantaneously released with the break of the limitation, which drive the ribbon to climb a ladder and jump on silica sand like the springtail.

Through ingenious structural design, CLCP nanocomposite actuators capable of more complex motions have been developed. Cai et al. developed a hybrid light-controlled robot featuring complicated tensegrity structures, where the stiff rods were compressed while the soft CNT/CLCP composite fibers were tensioned (**Figure** 22a).[214] The fibers near the base of support contracted and outputted a strong driving force upon irradiation, which led to the displacement of the barycenter and the rolling of the robot. The direction of rolling was determined by the position of the irradiated fiber, therefore multidirectional rolling along a zigzag path was achieved by selective and sequential irradiation.

He et al. designed a high-power oscillator featuring an antagonistic structure, which contained two monodomain CLCP layers and a sandwiched polydimethylsiloxane (PDMS) layer (Figure 22b).[215] The two CLCP layers incorporated with candle soot asynchronously contracted and relaxed upon light, similar to the antagonistic muscle pairs of the flying insects. The PDMS layer increased the resonate frequency and reduced the oscillator damping of the oscillator, mainly attributed to its higher modulus and lower viscoelasticity compared with CLCP layers. A built-in

self-oscillatory feedback loop was further built on the basis of the photothermal-induced bending and the self-shadowing-induced unbending upon constant irradiation. These designs of oscillator synergistically contributed to a remarkable output power density (33 W kg^{-1}) comparable to that of insect flight muscles (>29 W kg^{-1}), which allowed to propel a sailboat on the water.

Ware et al. achieved reversible collective entanglement and disentanglement with twist-aligned CLCP ribbons.[216] The initial flat ribbon took a spiral shape upon heating, which tended to entangle with adjacent ribbons. The length, offset angle θ, and packing density of CLCP ribbons were found to directly affect the mechanical interlocking between ribbons, thereby determining the degree of entanglement (Figure 22c). These ribbons were subsequently coated with an LM nanolayer. Under light irradiation, the photothermal ribbons became entangled, exhibiting enhanced electrical conductivity. Consequently, their interconnected pathways within a circuit conducted electricity to illuminate a bulb.

5. Conclusion and Perspectives

The CLCPs have been regarded as ideal materials for artificial muscles due to their sizable and highly designable deformation, but the research in this field has long been confined to a limited scope due to the complex synthesis and the alignment methods that are challenging for widespread adoption. Recently, the commercialized production of monomers, new materials chemistry, and application of 3D printing have significantly simplified the synthesis of CLCPs, and offered an easy-to-operate method to simultaneously regulate the mesogen alignment and geometries of LCP actuators. Therefore, the research boom of CLCPs toward nature-inspired actuators is virtually inevitable following these critical advancements.

The existing alignment methods are detailly combed, including the historic context, the required molecular structures of materials, the mechanism of alignment, and the representative nature-inspired actuators aligned by each method. Since the mesogen alignment and macroscopic structures have a decisive influence on the final achievable actuations of CLCPs, their synergistic regulation always remains a vital theme for the construction of actuators closer to natural organisms. Nevertheless, the programmability of mesogen alignment and macroscopic structures is generally contradictory for the existing alignment methods. For example, the surface-enforced alignment pioneers in regulating the mesogen alignment from 1D to complicated 3D patterns, but frustrates in the construction of macroscopic structures. The self-assembly allows to construct various macroscopic structures from 1D fibers to exquisite 3D structures, whereas suffers from the difficulty of attaining spatially distinguished mesogen alignment.

By comparison, the DIW serves as a viable middle ground that ensures to simultaneously pattern the mesogen alignment and construct 3D structures. Nevertheless, constrained by the low viscosity of precursors and the forming principles of deposition, the DIW still falls short of the regulation over z-axis mesogen alignment and direct construction of actuators with z-axis discontinuous structural characteristics. The magnetic field-assisted alignment facilitates the regulation of alignment patterns in LCP actuators with microscale features (10–100 µm), but the specialized challenges in the design and construction of magnetic field systems hinder their broader applications. The mechanical alignment is easy to operate and broadly available, but faces challenges in the precise patterning of alignment. In our opinion, the overarching goal for future alignment methods is to achieve desired alignment at any position within arbitrary 3D structures.

High output force, robust mechanical properties, and fast actuation speed are preferred by most practical usage scenarios of soft actuators and robots, which are quite challenging for pure LCP actuators. The nano-composition offers a convenient and highly efficient way to noticeably improve the actuation performance of LCP actuators, thus facilitating the design of robust LCP actuators featuring high work capacity. Currently, the studies of LCP nanocomposite actuators have mainly focused on the structural engineering and backend functions, while a gap persists in the systematic investigation of some fundamental yet critical material-related issues inherent to the nano-composition process, such as the interface issues and the regulation of multiphase structures.

Recent researches of LCP actuators have demonstrated a growing trend of interdisciplinary collaboration, which unlocks pathways toward practical deployable systems. We even envision that the LCPs will bring about new possibilities in next-generation soft robots with higher adaptability, autonomy, and operational capabilities in the near future, driven by the advances in materials engineering, fabrication techniques, robotics, and artificial intelligence.

Acknowledgements

X.Z. and Z.Y. contributed equally to this work. The authors were very grateful to D. J. Broer (Eindhoven University of Technology) for helpful discussion and advice. This work was financially supported by the National Key R&D Program of China (2023YFC3605700), the National Natural Science Foundation of China (52233001), the Innovation Program of Shanghai Municipal Education Commission (2023ZKZD07).

Conflict of Interest

The authors declare no conflict of interest.

Keywords

alignment regulation, liquid crystal polymer, nano-composition, soft actuator

Received: May 25, 2025
Revised: July 19, 2025
Published online:

[1] S. M. Mirvakili, I. W. Hunter, *Adv. Mater.* **2018**, *30*, 1704407.
[2] C. Kaspar, B. J. Ravoo, W. G. van der Wiel, S. V. Wegner, W. H. P. Pernice, *Nature* **2021**, *594*, 345.
[3] D. R. Yao, I. Kim, S. Yin, W. Gao, *Adv. Mater.* **2024**, *36*, 2308829.
[4] L. Feng, S. Li, Y. Li, H. Li, L. Zhang, J. Zhai, Y. Song, B. Liu, L. Jiang, D. Zhu, *Adv. Mater.* **2002**, *14*, 1857.
[5] M. Liu, S. Wang, Z. Wei, Y. Song, L. Jiang, *Adv. Mater.* **2009**, *21*, 665.
[6] Y. Zheng, H. Bai, Z. Huang, X. Tian, F. Q. Nie, Y. Zhao, J. Zhai, L. Jiang, *Nature* **2010**, *463*, 640.

[7] H. Chen, P. Zhang, L. Zhang, H. Liu, Y. Jiang, D. Zhang, Z. Han, L. Jiang, *Nature* **2016**, *532*, 85.
[8] M. Liu, S. Wang, L. Jiang, *Nat. Rev. Mater.* **2017**, *2*, 17036.
[9] X. Liu, X. Zhou, Z. Liu, *Acc. Chem. Res.* **2025**, *58*, 907.
[10] W. Feng, Q. He, L. Zhang, *Adv. Mater.* **2025**, *37*, 2312313.
[11] P. G. de Gennes, *Phys. Lett. A* **1969**, *28*, 725.
[12] T. J. White, D. J. Broer, *Nat. Mater.* **2015**, *14*, 1087.
[13] K. M. Herbert, H. E. Fowler, J. M. McCracken, K. R. Schlafmann, J. A. Koch, T. J. White, *Nat. Rev. Mater.* **2021**, *7*, 23.
[14] Z.-C. Jiang, Q. Liu, Y.-Y. Xiao, Y. Zhao, *Prog. Polym. Sci.* **2024**, *153*, 101829.
[15] T. H. Ware, Z. P. Perry, C. M. Middleton, S. T. Iacono, T. J. White, *ACS Macro Lett.* **2015**, *4*, 942.
[16] T. H. Ware, T. J. White, *Polym. Chem.* **2015**, *6*, 4835.
[17] C. P. Ambulo, J. J. Burroughs, J. M. Boothby, H. Kim, M. R. Shankar, T. H. Ware, *ACS Appl. Mater. Interfaces* **2017**, *9*, 37332.
[18] M. Lopez-Valdeolivas, D. Liu, D. J. Broer, C. Sanchez-Somolinos, *Macromol. Rapid. Commun.* **2018**, *39*, 1700710.
[19] A. Kotikian, R. L. Truby, J. W. Boley, T. J. White, J. A. Lewis, *Adv. Mater.* **2018**, *30*, 1706164.
[20] M. Chen, M. Gao, L. Bai, H. Zheng, H. J. Qi, K. Zhou, *Adv. Mater.* **2023**, *35*, 2209566.
[21] Y. Wang, J. Liu, S. Yang, *Appl. Phys. Rev.* **2022**, *9*, 011301.
[22] X. Peng, J. Zhang, P. Xiao, *Adv. Mater.* **2024**, *36*, 2400178.
[23] J. Küpfer, H. Finkelmann, *Makromol. Chem. Rapid Commun.* **1991**, *12*, 717.
[24] H. Finkelmann, E. Nishikawa, G. G. Pereira, M. Warner, *Phys. Rev. Lett.* **2001**, *87*, 015501.
[25] G. H. F. Bergmann, H. Finkelmann, V. Percec, M. Zhao, *Macromol. Rapid Commun.* **1997**, *18*, 353.
[26] T. Ohzono, K. Katoh, E. M. Terentjev, *Macromolecules* **2021**, *54*, 3678.
[27] F. Brommel, D. Kramer, H. Finkelmann, *Adv. Polym. Sci.* **2012**, *250*, 1.
[28] L. Yin, L. Han, F. Ge, X. Tong, W. Zhang, A. Soldera, Y. Zhao, *Angew. Chem., Int. Ed.* **2020**, *59*, 15129.
[29] M. Liu, L. Yin, Y. Zhao, *Macromolecules* **2023**, *56*, 9431.
[30] X. Zhao, Y. Chen, B. Peng, J. Wei, Y. Yu, *Angew. Chem., Int. Ed.* **2023**, *62*, 202300699.
[31] D. J. Broer, H. Finkelmann, K. Kondo, *Makromol. Chem.* **1988**, *189*, 185.
[32] D. J. Broer, J. Boven, G. N. Mol, G. Challa, *Makromol. Chem.* **1989**, *190*, 2255.
[33] J. Stohr, M. G. Samant, A. Cossy-Favre, J. Diaz, Y. Momoi, S. Odahara, T. Nagata, *Macromolecules* **1942**, *1998*, 31,
[34] S. Kumar, J. H. Kim, Y. Shi, *Phys. Rev. Lett.* **2005**, *94*, 077803.
[35] M. Kondo, Y. Yu, T. Ikeda, *Angew. Chem., Int. Ed.* **2006**, *118*, 1406.
[36] B. Sivaranjini, S. Umadevi, R. K. Khan, R. Pratibha, A. Dekshinamoorthy, S. Vijayaraghavan, V. Ganesh, *Liq. Cryst.* **2021**, *49*, 1246.
[37] X. Yu, V. V. Vashchenko, M. F. Prodanov, A. K. Srivastava, *J. Mol. Liq.* **2022**, *367*, 120535.
[38] J. M. Geary, J. W. Goodby, A. R. Kmetz, J. S. Patel, *J. Appl. Phys.* **1987**, *62*, 4100.
[39] B. A. Kowalski, V. P. Tondiglia, T. Guin, T. J. White, *Soft Matter* **2017**, *13*, 4335.
[40] L. Wang, W. Liu, L. Guo, B. Lin, X. Zhang, Y. Sun, H. Yang, *Polym. Chem.* **2017**, *8*, 1364.
[41] L. T. de Haan, V. Gimenez-Pinto, A. Konya, T. S. Nguyen, J. M. N. Verjans, C. Sánchez-Somolinos, J. V. Selinger, R. L. B. Selinger, D. J. Broer, A. P. H. J. Schenning, *Adv. Funct. Mater.* **2013**, *24*, 1251.
[42] H. Shahsavan, A. Aghakhani, H. Zeng, Y. Guo, Z. S. Davidson, A. Priimagi, M. Sitti, *Proc. Natl. Acad. Sci. USA* **2020**, *117*, 5125.
[43] W. Li, C. Lou, S. Liu, Q. Ma, G. Liao, K. C. F. Leung, X. Gong, H. Ma, S. Xuan, *Adv. Funct. Mater.* **2024**, *35*, 2414733.
[44] Y. Yu, M. Nakano, T. Ikeda, *Nature* **2003**, *425*, 145.
[45] X. Pang, J. A. Lv, C. Zhu, L. Qin, Y. Yu, *Adv. Mater.* **2019**, *31*, 1904224.
[46] T. Ikeda, M. Nakano, Y. Yu, O. Tsutsumi, A. Kanazawa, *Adv. Mater.* **2003**, *15*, 201.
[47] K. D. Harris, C. W. M. Bastiaansen, J. Lub, D. J. Broer, *Nano Lett.* **2005**, *5*, 1857.
[48] K. D. Harris, R. Cuypers, P. Scheibe, C. L. van Oosten, C. W. M. Bastiaansen, J. Lub, D. J. Broer, *J. Mater. Chem.* **2005**, *15*, 5043.
[49] W. Feng, A. Pal, T. Wang, Z. Ren, Y. Yan, Y. Lu, H. Yang, M. Sitti, *Adv. Funct. Mater.* **2023**, *33*, 2300731.
[50] Y. Sawaa, F. Yeb, K. Urayamaa, T. Takigawaa, V. Gimenez-Pintob, R. L. B. Selinger, J. V. Selinger, *Proc. Natl. Acad. Sci. USA* **2011**, *108*, 6364.
[51] K. M. Lee, T. J. Bunning, T. J. White, *Adv. Mater.* **2012**, *24*, 2839.
[52] S. Iamsaard, S. J. Asshoff, B. Matt, T. Kudernac, J. J. Cornelissen, S. P. Fletcher, N. Katsonis, *Nat. Chem.* **2014**, *6*, 229.
[53] G. N. Mol, K. D. Harris, C. W. M. Bastiaansen, D. J. Broer, *Adv. Funct. Mater.* **2005**, *15*, 1155.
[54] H. Shahsavan, S. M. Salili, A. Jakli, B. Zhao, *Adv. Mater.* **2015**, *27*, 6828.
[55] M. Pilz da Cunha, S. Ambergen, M. G. Debije, E. F. G. A. Homburg, J. M. J. den Toonder, A. P. H. J. Schenning, *Adv. Sci.* **2020**, *7*, 1902842.
[56] O. M. Wani, H. Zeng, A. Priimagi, *Nat. Commun.* **2017**, *8*, 15546.
[57] A. H. Gelebart, D. J Mulder, M. Varga, A. Konya, G. Vantomme, E. W. Meijer, R. L. B. Selinger, D. J. Broer, *Nature* **2017**, *546*, 632.
[58] W. M. Gibbons, P. J. Shannon, S.-T. Sun, B. J. Swetlin, *Nature* **1991**, *351*, 49.
[59] M. Schadt, K. Schmitt, V. Kozinkov, V. Chigrinov, *Jpn. J. Appl. Phys.* **1992**, *31*, 2155.
[60] H. Zeng, O. M. Wani, P. Wasylczyk, R. Kaczmarek, A. Priimagi, *Adv. Mater.* **2017**, *29*, 1701814.
[61] Y. Xia, G. Cedillo-Servin, R. D. Kamien, S. Yang, *Adv. Mater.* **2016**, *28*, 9637.
[62] L. T. de Haan, C. Sanchez-Somolinos, C. M. Bastiaansen, A. P. Schenning, D. J. Broer, *Angew. Chem., Int. Ed.* **2012**, *51*, 12469.
[63] M. E. McConney, A. Martinez, V. P. Tondiglia, K. M. Lee, D. Langley, I. I. Smalyukh, T. J. White, *Adv. Mater.* **2013**, *25*, 5880.
[64] T. H. Ware, M. E. McConney, J. J. Wie, V. P. Tondiglia, T. J. White, *Science* **2015**, *347*, 982.
[65] H. Aharonia, Y. Xia, X. Zhang, R. D. Kamiena, S. Yang, *Proc. Natl. Acad. Sci. USA* **2018**, *115*, 7206.
[66] T. Guin, M. J. Settle, B. A. Kowalski, A. D. Auguste, R. V. Beblo, G. W. Reich, T. J. White, *Nat. Commun.* **2018**, *9*, 2531.
[67] T. S. Hebner, K. Korner, C. N. Bowman, K. Bhattacharya, T. J. White, *Sci. Adv.* **2023**, *9*, ade1320
[68] S. R. Berrow, R. J. Mandle, T. Raistrick, M. Reynolds, H. F. Gleeson, *Macromolecules* **2024**, *57*, 5218.
[69] J. M. McCracken, J. D. Hoang, J. A. Herman, K. M. Lynch, T. J. White, *Adv. Mater. Technol.* **2023**, *8*, 2202067.
[70] T. Kimura, H. Sata, E. Ito, *Polym. J.* **1998**, *30*, 455.
[71] H. Hirschmann, P. M. S. Roberts, F. J. Davis, W. Guo, C. D. Hasson, G. R. Mitchell, *Polymer* **2001**, *42*, 7063.
[72] M.-H. Li, P. Keller, P.-A. Albouy, *Macromolecules* **2003**, *36*, 2284.
[73] M. H. Li, P. Keller, J. Yang, P. A. Albouy, *Adv. Mater.* **2004**, *16*, 1922.
[74] C. H. Legge, F. J. Davis, G. R. Mitchell, *J. Phys. II France* **1991**, *1*, 1253.
[75] R. A. M. Hikmet, *Macromolecules* **1992**, *25*, 5759.
[76] M. Brehmer, R. Zentel, G. Wagenblast, K. Siemensmeyer, *Macromol. Chem. Phys.* **1994**, *195*, 1891.
[77] H. Gruler, G. Meier, *Mol. Cryst. Liq. Cryst.* **1971**, *16*, 299.
[78] H. J. Deuling, W. Helfrich, *Appl. Phys. Lett.* **1974**, *25*, 129.
[79] C. Huang, Q. M. Zhang, A. Jákli, *Adv. Funct. Mater.* **2003**, *13*, 525.
[80] P. A. Kossyrev, J. Qi, N. V. Priezjev, R. A. Pelcovits, G. P. Crawford, *Appl. Phys. Lett.* **2002**, *81*, 2986.

[81] S. Ge, T. Zhao, M. Wang, L. Deng, B. Lin, X. Zhang, Y. Sun, H. Yang, E. Chen, *Soft Matter* **2017**, *13*, 5463.
[82] M. Li, P. Gong, Z. Zhang, L. Li, Y. Chen, Y. Qin, Y. Guo, R. Yang, J. Zhang, Y. Zhou, K. Xu, Y. Wang, H. Do, X. Jia, T. Cai, C.-T. Lin, N. Jiang, J. Yu, *Commun. Mater.* **2024**, *5*, 18.
[83] M. T. Brannum, A. M. Steele, M. C. Venetos, L. T. J. Korley, G. E. Wnek, T. J. White, *Adv. Optical Mater.* **2019**, *7*, 1801683.
[84] D. Liu, C. W. Bastiaansen, J. M. den Toonder, D. J. Broer, *Angew. Chem., Int. Ed.* **2012**, *51*, 892.
[85] R. J. H. van Raak, S. J. A. Houben, A. P. H. J. Schenning, D. J. Broer, *Adv. Mater. Technol.* **2022**, *7*, 2101619.
[86] T. Kimura, *Polym. J.* **2003**, *35*, 823.
[87] J. S. Moore, S. I. Stupp, *Macromolecules* **1987**, *20*, 273.
[88] S. Schuhladen, F. Preller, R. Rix, S. Petsch, R. Zentel, H. Zappe, *Adv. Mater.* **2014**, *26*, 7247.
[89] L. Pohl, R. Eidenschink, J. Krause, G. Weber, *Phys. Lett. A* **1978**, *65*, 169.
[90] A. Buguin, M.-H. Li, P. Silberzan, B. Ladoux, P. Keller, *J. Am. Chem. Soc.* **2006**, *128*, 1088.
[91] H. Yang, A. Buguin, J.-M. Taulemesse, K. Kaneko, S. Mery, A. Bergeret, P. Keller, *J. Am. Chem. Soc.* **2009**, *131*, 15000.
[92] Z. L. Wu, A. Buguin, H. Yang, J. M. Taulemesse, N. Le Moigne, A. Bergeret, X. Wang, P. Keller, *Adv. Funct. Mater.* **2013**, *23*, 3070.
[93] S. Li, M. Aizenberg, M. M. Lerch, J. Aizenberg, *Acc. Mater. Res.* **2023**, *4*, 1008.
[94] J. Cui, D. M. Drotlef, I. Larraza, J. P. Fernandez-Blazquez, L. F. Boesel, C. Ohm, M. Mezger, R. Zentel, A. del Campo, *Adv. Mater.* **2012**, *24*, 4601.
[95] Y. Yao, J. T. Waters, A. V. Shneidman, J. Cui, X. Wang, N. K. Mandsberg, S. Li, A. C. Balazs, J. Aizenberg, *Proc. Natl. Acad. Sci. USA* **2018**, *115*, 12950.
[96] M. Tabrizi, T. H. Ware, M. R. Shankar, *ACS Appl. Mater. Interfaces* **2019**, *11*, 28236.
[97] S. Li, M. M. Lerch, J. T. Waters, B. Deng, R. S. Martens, Y. Yao, D. Y. Kim, K. Bertoldi, A. Grinthal, A. C. Balazs, J. Aizenberg, *Nature* **2022**, *605*, 76.
[98] J. E. Taylor, A. Romo-Uribe, M. R. Libera, *Macromolecules* **2002**, *35*, 1751.
[99] S. Kenig, *Polym. Engin. Sci.* **2004**, *29*, 1136.
[100] H. N. Yoon, L. F. Charbonneau, G. W. Calundann, *Adv. Mater.* **2004**, *4*, 206.
[101] V. M. Ugaz, W. R. Burghardt, W. Zhou, J. A. Kornfield, *J. Rheol.* **2001**, *45*, 1029.
[102] G. E. Bauman, J. A. Koch, T. J. White, *Soft Matter* **2022**, *18*, 3168.
[103] R. Telles, A. Kotikian, G. Freychet, M. Zhernenkov, P. Wasik, B. M. Yavitt, J. L. Barrera, C. C. Cook, R. Pindak, E. C. Davidson, J. A. Lewis, *Proc. Natl. Acad. Sci. USA* **2025**, *122*, 2414960122.
[104] C. Ohm, C. Serra, R. Zentel, *Adv. Mater.* **2009**, *21*, 4859.
[105] C. Ohm, M. Morys, F. R. Forst, L. Braun, A. Eremin, C. Serra, R. Stannarius, R. Zentel, *Soft Matter* **2011**, *7*, 3730.
[106] M. Liu, L. Jin, S. Yang, Y. Wang, C. B. Murray, S. Yang, *Adv. Mater.* **2023**, *35*, 2208613.
[107] G. G. Viola, D. G. Baird, *J. Rheol.* **1986**, *30*, 601.
[108] J. Naciri, A. Srinivasan, H. Jeon, N. Nikolov, P. Keller, B. R. Ratna, *Macromolecules* **2003**, *36*, 8499.
[109] S. Krause, R. Dersch, J. H. Wendorff, H. Finkelmann, *Macromol. Rapid Commun.* **2007**, *28*, 2062.
[110] J. P. Canejo, J. P. Borges, M. H. Godinho, P. Brogueira, P. I. C. Teixeira, E. M. Terentjev, *Adv. Mater.* **2008**, *20*, 4821.
[111] M. Tokita, G. Sugiyama, S. Masuyama, T. Ishii, S. Kang, J. Watanabe, *Macromolecules* **2009**, *42*, 8406.
[112] M. Tokita, A. Ikoma, T. Ishii, S. Kang, J. Watanabe, T. Matsuoka, *Macromolecules* **2012**, *45*, 4857.
[113] T. Tepe, M. F. Schulz, J. Zhao, M. Tirrell, F. S. Bates, *Macromolecules* **1995**, *28*, 3008.
[114] R. M. Kannan, J. A. Kornfield, N. Schwenk, C. Boeffel, *Adv. Mater.* **2004**, *6*, 214.
[115] S. Rendon, W. R. Burghardt, *Macromolecules* **2007**, *40*, 6624.
[116] S. Gantenbein, K. Masania, W. Woigk, J. P. W. Sesseg, T. A. Tervoort, A. R. Studart, *Nature* **2018**, *561*, 226.
[117] W. Hou, J. Wang, J. A. Lv, *Adv. Mater.* **2023**, *35*, 2211800.
[118] M. Srinivasarao, *Int. J. Mod. Phys. B* **1995**, *09*, 2515.
[119] A. Romo-Uribe, A. H. Windle, *Macromolecules* **1996**, *29*, 6246.
[120] J. H. Lee, S. Oh, I. Jeong, Y. J. Lee, M. C. Kim, J. S. Park, K. Hyun, T. H. Ware, S. Ahn, *Sci. Adv.* **2025**, *11*, adt7613.
[121] A. H. Gelebart, M. Mc Bride, A. P. H. J. Schenning, C. N. Bowman, D. J. Broer, *Adv. Funct. Mater.* **2016**, *26*, 5322.
[122] L. Liu, M. del Pozo, F. Mohseninejad, M. G. Debije, D. J. Broer, A. P. H. J. Schenning, *Adv. Optical Mater.* **2020**, *8*, 2000732.
[123] Y. Wu, Q. An, J. Yin, T. Hua, H. Xie, G. Li, H. Tang, *Colloid Polym. Sci.* **2008**, *286*, 897.
[124] X. Zheng, Y. Jia, A. Chen, *Nat. Commun.* **2021**, *12*, 4875.
[125] Y. Liu, C. Zhu, Y. Zhao, X. Qing, F. Wang, D. Deng, J. Wei, Y. Yu, *Adv. Mater. Interfaces* **2019**, *6*, 1901158.
[126] S. Li, H. Bai, Z. Liu, X. Zhang, C. Huang, L. W. Wiesner, M. Silberstein, R. F. Shepherd, *Sci. Adv.* **2021**, *7*, abg3677.
[127] L. C. Sawyer, M. Jaffe, *J. Polym. Sci.* **1986**, *21*, 1897.
[128] Z. Wang, Z. Wang, Y. Zheng, Q. He, Y. Wang, S. Cai, *Sci. Adv.* **2020**, *6*, abc0034.
[129] J. A. Lewis, *Adv. Funct. Mater.* **2006**, *16*, 2193.
[130] A. Kotikian, C. McMahan, E. C. Davidson, J. M. Muhammad, R. D. Weeks, C. Daraio, J. A. Lewis, *Sci. Robot.* **2019**, *4*, aax7044.
[131] G. Long, Y. Deng, W. Zhao, G. Zhou, D. J. Broer, B. L. Feringa, J. Chen, *J. Am. Chem. Soc.* **2024**, *146*, 13894.
[132] S. Leanza, J. Lu-Yang, B. Kaczmarski, S. Wu, E. Kuhl, R. R. Zhao, *Adv. Funct. Mater.* **2024**, *34*, 2400396.
[133] X. Feng, L. Wang, Z. Xue, C. Xie, J. Han, Y. Pei, Z. Zhang, W. Guo, B. Lu, *Sci. Adv.* **2024**, *10*, adk3854.
[134] M. O. Saed, C. P. Ambulo, H. Kim, R. De, V. Raval, K. Searles, D. A. Siddiqui, J. M. O. Cue, M. C. Stefan, M. R. Shankar, T. H. Ware, *Adv. Funct. Mater.* **2018**, *29*, 1806412.
[135] A. Kotikian, A. A. Watkins, G. Bordiga, A. Spielberg, Z. S. Davidson, K. Bertoldi, J. A. Lewis, *Adv. Mater.* **2024**, *36*, 2310743.
[136] D. J. Roach, X. Sun, X. Peng, F. Demoly, K. Zhou, H. J. Qi, *Adv. Funct. Mater.* **2022**, *32*, 2203236.
[137] X. Peng, S. Wu, X. Sun, L. Yue, S. M. Montgomery, F. Demoly, K. Zhou, R. R. Zhao, H. J. Qi, *Adv. Mater.* **2022**, *34*, 2204890.
[138] Q. Wang, X. Tian, D. Zhang, Y. Zhou, W. Yan, D. Li, *Nat. Commun.* **2023**, *14*, 3869.
[139] C. M. Yakacki, M. Saed, D. P. Nair, T. Gong, S. M. Reed, C. N. Bowman, *RSC Adv.* **2015**, *5*, 18997.
[140] Z. Pei, Y. Yang, Q. Chen, E. M. Terentjev, Y. Wei, Y. Ji, *Nat. Mater.* **2014**, *13*, 36.
[141] Z. Zheng, W. Ma, J. Li, Y. Ma, J. Hu, M. H. Li, *Adv. Funct. Mater.* **2024**, *34*, 2410235.
[142] Y. Xu, Y. Huang, J. Wang, S. Huang, H. Yang, Q. Li, *Angew. Chem., Int. Ed.* **2025**, *64*, 202423584.
[143] Z. Wang, M. Si, J. Han, Y. Wu, T. Zhang, K. Yin, T. Chen, *Adv. Mater.* **2025**, *37*, 2501815.
[144] L. Liu, M. H. Liu, L. L. Deng, B. P. Lin, H. Yang, *J. Am. Chem. Soc.* **2017**, *139*, 11333.
[145] T. Wen, T. Ma, J. Qian, Z. Song, X. Jiang, Y. Yao, *Nat. Commun.* **2024**, *15*, 10821.
[146] Z. Liu, H. K. Bisoyi, Y. Huang, M. Wang, H. Yang, Q. Li, *Angew. Chem., Int. Ed.* **2022**, *61*, 202115755.
[147] M. Wang, B. P. Lin, H. Yang, *Nat. Commun.* **2016**, *7*, 13981.
[148] Z. Yang, L. Zhang, *Macromolecules* **2023**, *56*, 7551.

[149] M. Zhang, A. Pal, X. Lyu, Y. Wu, M. Sitti, *Nat. Mater.* **2024**, *23*, 560.
[150] Z. Z. Nie, B. Zuo, M. Wang, S. Huang, X. M. Chen, Z. Y. Liu, H. Yang, *Nat. Commun.* **2021**, *12*, 2334.
[151] Z. Deng, K. Li, A. Priimagi, H. Zeng, *Nat. Mater.* **2024**, *23*, 1728.
[152] Y. Huang, H. K. Bisoyi, S. Huang, M. Wang, X. M. Chen, Z. Liu, H. Yang, Q. Li, *Angew. Chem., Int. Ed.* **2021**, *60*, 11247.
[153] Y. Huang, Y. Xu, H. K. Bisoyi, Z. Liu, J. Wang, Y. Tao, T. Yang, S. Huang, H. Yang, Q. Li, *Adv. Mater.* **2023**, *35*, 2304378.
[154] X. Zhou, B. Jin, Z. Zhu, J. Wu, Q. Zhao, G. Chen, *Angew. Chem., Int. Ed.* **2024**, *63*, 202409182.
[155] Z. C. Jiang, Y. Y. Xiao, L. Yin, L. Han, Y. Zhao, *Angew. Chem., Int. Ed.* **2020**, *59*, 4925.
[156] X. Huang, L. Qin, J. Wang, X. Zhang, B. Peng, Y. Yu, *Adv. Funct. Mater.* **2022**, *32*, 2208312.
[157] Y. Wu, Y. Yang, X. Qian, Q. Chen, Y. Wei, Y. Ji, *Angew. Chem., Int. Ed.* **2020**, *59*, 4778.
[158] M. C. Escobar, T. J. White, *Adv. Mater.* **2024**, *36*, 2401140.
[159] S. J. D. Lugger, D. J. Mulder, A. Schenning, *Angew. Chem., Int. Ed.* **2022**, *61*, 202115166.
[160] S. J. D. Lugger, T. A. P. Engels, R. Cardinaels, T. Bus, D. J. Mulder, A. P. H. J. Schenning, *Adv. Funct. Mater.* **2023**, *33*, 2306853.
[161] Y. Wang, J. Sun, W. Liao, Z. Yang, *Adv. Mater.* **2022**, *34*, 2107840.
[162] Q. Liu, Z. C. Jiang, X. Jiang, J. Zhao, Y. Zhang, Y. Liu, J. B. Hou, Y. Y. Xiao, W. Pu, Y. Zhao, *Angew. Chem., Int. Ed.* **2025**, *137*, 202500527.
[163] X. Zhou, B. Yang, N. Zheng, *Acta Polym. Sin.* **2024**, *55*, 614.
[164] L. Yue, E. P. J. Ambergen, S. J. D. Lugger, A. R. Peeketi, R. K. Annabattula, A. Schenning, M. G. Debije, *Adv. Mater.* **2024**, *36*, 2402559.
[165] X. Qian, Q. Chen, Y. Yang, Y. Xu, Z. Li, Z. Wang, Y. Wu, Y. Wei, Y. Ji, *Adv. Mater.* **2018**, *30*, 1801103.
[166] N. A. Traugutt, D. Mistry, C. Luo, K. Yu, Q. Ge, C. M. Yakacki, *Adv. Mater.* **2020**, *32*, 2000797.
[167] G. Chen, B. Jin, Y. Shi, Q. Zhao, Y. Shen, T. Xie, *Adv. Mater.* **2022**, *34*, 2201679.
[168] W. Peng, P. Zhao, X. Zhou, X. Liang, X. Zhang, B. Jin, G. Chen, Q. Zhao, T. Xie, *Sci. Adv.* **2024**, *10*, adp4814.
[169] B. Jin, J. Liu, Y. Shi, G. Chen, Q. Zhao, S. Yang, *Adv. Mater.* **2022**, *34*, 2107855.
[170] J. Lv, Y. Liu, J. Wei, E. Chen, L. Qin, Y. Yu, *Nature* **2016**, *537*, 179.
[171] Q. Liu, Y. Liu, J. Lv, E. Chen, Y. Yu, *Adv. Intell. Syst.* **2019**, *1*, 1900060.
[172] B. Xu, C. Zhu, L. Qin, J. Wei, Y. Yu, *Small* **2019**, *15*, 1901847.
[173] X. Pang, L. Qin, B. Xu, Q. Liu, Y. Yu, *Adv. Funct. Mater.* **2020**, *30*, 2002451.
[174] X. Qing, Y. Liu, J. Wei, R. Zheng, C. Zhu, Y. Yu, *Adv. Optical Mater.* **2018**, *7*, 1801494.
[175] B. Peng, X. Chen, G. Yu, F. Xu, R. Yang, Z. Yu, J. Wei, G. Zhu, L. Qin, J. Zhang, Q. Shen, Y. Yu, *Adv. Funct. Mater.* **2023**, *33*, 2214172.
[176] X. Zhao, Z. Yang, X. Zhang, X. Liu, Y. Pu, L. Qin, J. Wei, Y. Yu, *Adv. Optical Mater.* **2025**, *13*, 2403469.
[177] L. Zhang, Z. Yang, W. Xia, J. Li, H. Yang, S. Yang, E. Chen, *J. Am. Chem. Soc.* **2024**, *146*, 31221.
[178] Z. Yang, J. Li, X. Chen, Y. Fan, J. Huang, H. Yu, S. Yang, E. Chen, *Adv. Mater.* **2023**, *35*, 2211648.
[179] Y. Fan, Z. Yang, J. Wu, L. Zhao, W. Xia, L. Zhang, J. Wang, J. Chen, M. Sun, J. Li, S. Yang, E. Chen, *Acta Polym. Sin.* **2023**, *54*, 1468.
[180] J. Jeon, J.-C. Choi, H. Lee, W. Cho, K. Lee, J. G. Kim, J.-W. Lee, K.-I. Joo, M. Cho, H.-R. Kim, J. J. Wie, *Mater. Today* **2021**, *49*, 97.
[181] A. H. Gelebart, G. Vantomme, E. W. Meijer, D. J. Broer, *Adv. Mater.* **2017**, *29*, 1606712.
[182] H. Wu, J. Lou, B. Zhang, Y. Dai, K. Li, *Appl. Math. Mech.-Engl. Ed.* **2024**, *45*, 337.
[183] W. Wang, X. Sun, W. Wu, H. Peng, Y. Yu, *Angew. Chem., Int. Ed.* **2012**, *51*, 4644.
[184] H. Kim, J. A. Lee, C. P. Ambulo, H. B. Lee, S. H. Kim, V. V. Naik, C. S. Haines, A. E. Aliev, R. Ovalle-Robles, R. H. Baughman, T. H. Ware, *Adv. Funct. Mater.* **2019**, *29*, 1905063.
[185] H. Chen, X. Yao, H. Qin, H. P. Cong, S. H. Yu, *Adv. Funct. Mater.* **2024**, *35*, 2412728.
[186] L. Zadoina, B. Lonetti, K. Soulantica, A. F. Mingotaud, M. Respaud, B. Chaudret, M. Mauzac, *J. Mater. Chem.* **2009**, *19*, 8075.
[187] A. K. Srivastava, W. Zhang, J. Schneider, A. L. Rogach, V. G. Chigrinov, H. S. Kwok, *Adv. Mater.* **2017**, *29*, 1701091.
[188] J. Sang, J. Zhang, H. Feng, J. Sun, J. Shang, Y. Zhang, S. Zhao, K. Neyts, V. Chigrinov, *Adv. Optical Mater.* **2022**, *10*, 2200950.
[189] O. Riou, B. Lonetti, R. P. Tan, J. Harmel, K. Soulantica, P. Davidson, A. F. Mingotaud, M. Respaud, B. Chaudret, M. Mauzac, *Angew. Chem., Int. Ed.* **2015**, *54*, 10811.
[190] O. Riou, B. Lonetti, P. Davidson, R. P. Tan, B. Cormary, A. F. Mingotaud, E. Di Cola, M. Respaud, B. Chaudret, K. Soulantica, M. Mauzac, *J. Phys. Chem. B* **2014**, *118*, 3218.
[191] Y. Wang, A. Dang, Z. Zhang, R. Yin, Y. Gao, L. Feng, S. Yang, *Adv. Mater.* **2020**, *32*, 2004270.
[192] Y. Yang, W. Zhan, R. Peng, C. He, X. Pang, D. Shi, T. Jiang, Z. Lin, *Adv. Mater.* **2015**, *27*, 6376.
[193] L. Yang, K. Setyowati, A. Li, S. Gong, J. Chen, *Adv. Mater.* **2008**, *20*, 2271.
[194] Y. Ji, Y. Y. Huang, R. Rungsawang, E. M. Terentjev, *Adv. Mater.* **2010**, *22*, 3436.
[195] Y. Wang, R. Yin, L. Jin, M. Liu, Y. Gao, J. Raney, S. Yang, *Adv. Funct. Mater.* **2022**, *33*, 2210614.
[196] S. Vasanji, M. G. Scarfo, A. Alyami, T. H. Mekonnen, P. Hajireza, M. O. Saed, A. Jakli, H. Shahsavan, *Adv. Mater.* **2025**, 2504592.
[197] A. W. Hauser, D. Liu, K. C. Bryson, R. C. Hayward, D. J. Broer, *Macromolecules* **2016**, *49*, 1575.
[198] M. Wang, S. M. Sayed, L.-X. Guo, B.-P. Lin, X.-Q. Zhang, Y. Sun, H. Yang, *Macromolecules* **2016**, *49*, 663.
[199] X. Lu, H. Zhang, G. Fei, B. Yu, X. Tong, H. Xia, Y. Zhao, *Adv. Mater.* **2018**, *30*, 1706597.
[200] L. Zhang, J. Pan, C. Gong, A. Zhang, *J. Mater. Chem. C* **2019**, *7*, 10663.
[201] M. J. Ford, C. P. Ambulo, T. A. Kent, E. J. Markvicka, C. F. Pan, J. Malen, T. H. Ware, C. Majidi, *Proc. Natl. Acad. Sci. USA* **2019**, *116*, 21438.
[202] H. Lu, Z. Nie, H. K. Bisoyi, M. Wang, S. Huang, X. Chen, Z. Liu, H. Yang, *Sci. China Mater.* **2022**, *65*, 1679.
[203] H. Kim, J. M. Boothby, S. Ramachandran, C. D. Lee, T. H. Ware, *Macromolecules* **2017**, *50*, 4267.
[204] M. Javed, T. Corazao, M. O. Saed, C. P. Ambulo, Y. Li, M. R. Kessler, T. H. Ware, *ACS Appl. Mater. Interfaces* **2022**, *14*, 35087.
[205] I. H. Kim, S. Choi, J. Lee, J. Jung, J. Yeo, J. T. Kim, S. Ryu, S. K. Ahn, J. Kang, P. Poulin, S. O. Kim, *Nat. Nanotechnol.* **2022**, *17*, 1198.
[206] M. Yang, Y. Xu, X. Zhang, H. K. Bisoyi, P. Xue, Y. Yang, X. Yang, C. Valenzuela, Y. Chen, L. Wang, W. Feng, Q. Li, *Adv. Funct. Mater.* **2022**, *32*, 2201884.
[207] Y. Sun, L. Wang, Z. Zhu, X. Li, H. Sun, Y. Zhao, C. Peng, J. Liu, S. Zhang, M. Li, *Adv. Mater.* **2023**, *35*, 2302824.
[208] Z. Wang, M. Si, J. Han, Y. Shen, G. Yin, K. Yin, P. Xiao, T. Chen, *Angew. Chem., Int. Ed.* **2025**, *64*, 202416095.
[209] Y. Wang, Q. Guan, D. Lei, R. E Neisiany, Y. Guo, S. Gu, Z. You, *ACS Nano* **2022**, *16*, 19393.
[210] X. Yang, Y. Chen, X. Zhang, P. Xue, P. Lv, Y. Yang, L. Wang, W. Feng, *Nano Today* **2022**, *43*, 101419.
[211] Y. Chi, Y. Li, Y. Zhao, Y. Hong, Y. Tang, J. Yin, *Adv. Mater.* **2022**, *34*, 2110384.

[212] J. Wang, T. Zhao, Y. Fan, H. Wu, J. a. Lv, *Adv. Funct. Mater.* **2022**, *33*, 2209798.
[213] J. Hu, Z. Nie, M. Wang, Z. Liu, S. Huang, H. Yang, *Angew. Chem., Int. Ed.* **2023**, *62*, 202218227.
[214] Z. Wang, K. Li, Q. He, S. Cai, *Adv. Mater.* **2019**, *31*, 1806849.
[215] Y. Zhao, Z. Liu, P. Shi, C. Chen, Y. Alsaid, Y. Yan, X. He, *Nat. Mater.* **2025**, *24*, 116.
[216] M. K. Abdelrahman, R. J. Wagner, M. S. Kalairaj, M. Zadan, M. H. Kim, L. K. Jang, S. Wang, M. Javed, A. Dana, K. A. Singh, S. E. Hargett, A. K. Gaharwar, C. Majidi, F. J. Vernerey, T. H. Ware, *Nat. Mater.* **2024**, *23*, 281.

Xiaoyu Zhang is currently a Ph.D. student in the College of Smart Materials and Future Energy, Fudan University (China). She received her B.S. degree in the College of Polymer Science and Engineering at Sichuan University (China) in 2021. Her research interests focus on the design of liquid crystal polymers and soft actuators.

Ziyue Yang is currently a Ph.D. student in the College of Smart Materials and Future Energy, Fudan University (China). She received her B.S. (2020) and M.S. (2023) degrees in the School of Chemistry and Molecular Engineering at East China Normal University (China). Her research interests focus on the design of liquid crystal polymers and soft actuators.

Yanlei Yu is a professor in the College of Smart Materials and Future Energy at Fudan University, China. She graduated in applied chemistry from Anhui University in 1993 and obtained her M.S. degree in polymer chemistry and physics from the University of Science and Technology of China in 1996. She gained her Ph.D. degree in environmental chemistry and engineering from Tokyo Institute of Technology and was promoted to full professor at Fudan University in 2004. Her research interests focus on the development of photodeformable smart materials and liquid crystal polymers.